

**This item is the archived peer-reviewed author-version of:**

Early functional connectivity deficits and progressive microstructural alterations in the TgF344-AD rat model of Alzheimers disease : a longitudinal MRI study

**Reference:**

Anckaerts Cynthia, Blockx Ines, Summer Priska, Michael Johanna, Hamaide Julie, Kreutzer Christina, Boutin Hervé, Couillard-Després Sébastien, Verhoye Marleen, Van Der Linden Anne-Marie.- Early functional connectivity deficits and progressive microstructural alterations in the TgF344-AD rat model of Alzheimers disease : a longitudinal MRI study  
Neurobiology of disease - ISSN 0969-9961 - 124(2019), p. 93-107  
Full text (Publisher's DOI): <https://doi.org/10.1016/J.NBD.2018.11.010>  
To cite this reference: <https://hdl.handle.net/10067/1555640151162165141>

# Early functional connectivity deficits and progressive microstructural alterations in the TgF344-AD rat model of Alzheimer's Disease: a longitudinal MRI study.

Cynthia Anckaerts<sup>a\*</sup>, Ines Blockx<sup>a</sup>, Priska Summer<sup>b</sup>, Johanna Michael<sup>b,c</sup>, Julie Hamaide<sup>a</sup>, Christina Kreutzer<sup>b</sup>, Hervé Boutin<sup>d</sup>, Sébastien Couillard-Després<sup>b</sup>, Marleen Verhoye<sup>a</sup>, Annemie Van der Linden<sup>a</sup>

<sup>a</sup>Bio-Imaging Lab, University of Antwerp, Universiteitsplein 1, Wilrijk 2610, Antwerp, Belgium;

<sup>b</sup>Institute of Experimental Neuroregeneration; Spinal Cord Injury and Tissue Regeneration Centre Salzburg, Paracelsus Medical University, Strubergasse 22, 5020 Salzburg, Austria;

<sup>c</sup>Institute of Molecular Regenerative Medicine; Spinal Cord Injury and Tissue Regeneration Centre Salzburg, Paracelsus Medical University, Strubergasse 22, 5020 Salzburg, Austria;

<sup>d</sup>Wolfson Molecular Imaging Centre, Faculty of Biology, Medicine and Health and Manchester Academic Health Sciences Centre, University of Manchester, Manchester, M20 3LJ, UK.

\* Corresponding author: Cynthia Anckaerts, [cynthia.anckaerts@uantwerpen.be](mailto:cynthia.anckaerts@uantwerpen.be)

Bio-Imaging Lab, University of Antwerp, Universiteitsplein 1, 2610 Wilrijk, Belgium

## **Keywords**

Alzheimer's disease, TgF344-AD, resting state fMRI, rsfMRI, diffusion tensor imaging, DTI, functional connectivity, FC, amyloid plaque

1 **Abstract**

2 The development and characterization of new improved animal models is pivotal in Alzheimer's  
3 Disease (AD) research, since valid models enable the identification of early pathological processes,  
4 which are often not accessible in patients, as well as subsequent target discovery and evaluation. The  
5 TgF344-AD rat model of AD, bearing mutant human amyloid precursor protein (APP<sup>swe</sup>) and  
6 Presenilin 1 (PSEN1 $\Delta$ E9) genes, has been described to manifest the full spectrum of AD pathology  
7 similar to human AD, *i.e.* progressive cerebral amyloidosis, tauopathy, neuronal loss and age-  
8 dependent cognitive decline. Here, AD-related pathology in female TgF344-AD rats was examined  
9 longitudinally between 6 and 18 months by means of complementary translational MRI techniques:  
10 resting state functional MRI (rsfMRI) to evaluate functional connectivity (FC) and diffusion tensor  
11 imaging (DTI) to assess the microstructural integrity. Additionally, an evaluation of macroscopic  
12 changes (3D anatomical MRI) and an image-guided validation of *ex vivo* pathology were performed.  
13 We identified slightly decreased FC at 6 months followed by severe and widespread hypoconnectivity  
14 at 10 months of age as the earliest detectable pathological MRI hallmark. This initial effect was  
15 followed by age-dependent progressive microstructural deficits in parallel with age-dependent *ex vivo*  
16 AD pathology, without signs of macroscopic alterations such as hippocampal atrophy.  
17 This longitudinal MRI study in the TgF344-AD rat model of AD revealed early rsfMRI and DTI  
18 abnormalities as seen in human AD patients. The characterization of AD pathology in this rat model  
19 using non-invasive MRI techniques further highlights the translational value of this model, as well as  
20 its use for potential treatment evaluation.

## 21 INTRODUCTION

22 Alzheimer's disease (AD) is the most common cause of dementia and one of the most important  
23 causes of morbidity among the aging population. Since one of the hallmarks of AD is extracellular  
24 accumulation of amyloid  $\beta$  (A $\beta$ ) peptides, this has been a common and popular target for the  
25 development of transgenic mouse models of AD. The use of these transgenic mouse models has led  
26 to new insights in relation to the so-called "amyloid cascade hypothesis" (Barage and Sonawane, 2015;  
27 Hardy and Higgins, 1992). Although transgenic mouse models have been proven highly valuable in  
28 elucidating several pathological mechanisms involved in AD, they do not demonstrate robust A $\beta$   
29 plaque deposition in combination with distinct tauopathy and neuronal loss unless additional human  
30 transgenes are included, *e.g.* triple transgenic AD mouse model (Do Carmo and Cuellar, 2013). Because  
31 rats are physiologically, genetically and morphologically closer to humans, they offer numerous  
32 advantages compared to mice (Gibbs et al., 2004; Jacob and Kwitek, 2002). Cohen and colleagues  
33 developed a new transgenic rat model of AD, the TgF344-AD rat model, bearing mutant human  
34 amyloid precursor protein (APP<sub>Swe</sub>) and Presenilin 1 (PSEN1 $\Delta$ E9) genes (Cohen et al., 2013). According  
35 to this initial publication, TgF344-AD rats demonstrate strong age-dependent amyloidosis as well as  
36 tauopathy and apoptotic loss of neurons, coincident with progressive cognitive decline between 6 and  
37 26 months of age. Further research has shown that already at 4 months of age, this rat model shows  
38 enhanced anxiety-like behaviour (Pentkowski et al., 2018). As early as 6 months of age, the TgF344-  
39 AD rat model presents reduced basal synaptic transmission in entorhinal-hippocampal synapses. An  
40 effect which is followed by dysfunction of hippocampal CA3-CA1 synapses at 9 months in males and  
41 only at 12 months in females (Smith and McMahon, 2018). At 9 months of age, also neurovascular  
42 dysfunction has been observed using two-photon microscopy and electrophysiological measures  
43 (Bazzigaluppi et al., 2017; Joo et al., 2017). Another study described evidence of early tau  
44 accumulation and progressive dysfunction of the noradrenergic system in this rat model between 6  
45 and 16 months of age (Rorabaugh et al., 2017). Interestingly, it has been shown that targeting  
46 noradrenergic dysfunction improves performance in the Morris Water maze in 16 month old animals

47 (Rorabaugh et al., 2017) and that treatment aimed at preserving neuronal survival prevents  
48 depressive-like behaviour at 16 months as well as cognitive deficits at 24 months (Voorhees et al.,  
49 2017). In contrast to other rodent models with merely a single pathological aspect of AD (*e.g.*  
50 amyloidosis), this rat model is currently recognized as a highly clinically relevant model as it entails  
51 AD-related pathology much akin to the spatiotemporal pattern of human AD pathology (Braak and  
52 Braak, 1991; Braak and Braak, 1995; Thal et al., 2002).

53

54 Today, not only cerebrospinal fluid (CSF) biomarkers, but also neuroimaging techniques such as  
55 positron emission tomography (PET) and magnetic resonance imaging (MRI) have acquired a central  
56 position in ascertaining the diagnosis of AD, providing insights into the effects of AD pathology and its  
57 temporal and spatial evolution (Johnson et al., 2012). Structural and functional magnetic resonance  
58 imaging studies have gained immensely in popularity in the study of early events of AD. As such,  
59 structural MRI is used for the detection of atrophy due to dendritic and neuronal loss in brain regions  
60 such as the entorhinal cortex, hippocampus and posterior cingulate cortex (Dubois et al., 2007;  
61 Johnson et al., 2012). Beside macroscopic volume loss, microstructural changes can also be observed  
62 using diffusion tensor imaging (DTI) starting at earlier stages of the disease (Nir et al., 2013; Weston  
63 et al., 2015). Ever since the work of Brun and Englund in 1986, it is known that microscopic white  
64 matter changes are present in AD (Brun and Englund, 1986; Gold et al., 2012). Although many studies  
65 focus on white matter, grey matter changes also exist in early stages of AD in several brain regions,  
66 including the hippocampus, posterior cingulate cortex and subcortical regions, preceding  
67 macrostructural atrophy (Weston et al., 2015). Next to the observation of alterations in  
68 microstructural integrity in AD, markers of neuronal function have been shown to be useful in  
69 detecting AD-related pathology (Balachandar et al., 2015; Hoozemans et al., 2006) as the earliest  
70 pathological alterations include the presence of soluble A $\beta$  and inflammation leading to synaptic  
71 deficits (Busche et al., 2012; Ewers et al., 2011; Rao et al., 2012; Selkoe, 2002; Shankar et al., 2007).  
72 For this, resting state functional MRI (rsfMRI) has been proven to be a valuable technique by allowing

73 the observation of functional connectivity (FC) based on the blood oxygenation level dependent  
74 (BOLD) signal. FC refers to networks of spatially distributed, but functionally connected brain regions  
75 and is considered as an indirect measure of trans-synaptic activity (van den Heuvel and Hulshoff Pol,  
76 2010). As such, altered FC has been observed in brain regions important for learning and memory,  
77 even before appreciable plaque deposition and the onset of clinical symptoms (Balachandar et al.,  
78 2015; Chase, 2014; Sheline and Raichle, 2013).

79 Within the present study, we aimed to longitudinally examine the transgenic TgF344-AD rat model of  
80 AD using these complementary non-invasive MRI tools, in order to enable future preclinical and  
81 translational AD research. More specifically, we studied i) functional connectivity using rsfMRI, ii)  
82 white and grey matter integrity using DTI, and iii) macrostructural changes using 3D anatomical MRI.  
83 Because AD is more common in women, female TF344-AD rats were selected and studied  
84 longitudinally between 6 and 18 months of age, *i.e.* from early stages up to more advanced stages of  
85 the disease. We hypothesized that the early pathological processes in AD that lead to synaptic deficits  
86 could be reflected by aberrant FC measured by rsfMRI. Additionally, we hypothesized that minor  
87 (early-stage) and major (late-stage) structural changes could be detected using DTI prior to  
88 macroscopic alterations. Lastly, we included *ex vivo* examinations to validate the underlying AD  
89 pathology.

90

## 91 **MATERIAL & METHODS**

### 92 ***Ethical statement***

93 All procedures were performed in strict accordance with the European Directive 2010/63/EU on the  
94 protection of animals used for scientific purposes. The protocols were approved by the Committee on  
95 Animal Care and Use at the University of Antwerp, Belgium (permit number 2016-17) and all efforts  
96 were made to ensure animal well-being.

97

### 98 ***Animals***

99 TgF344-AD and WT littermates breeding pairs were purchased from the group of Prof. Terrence Town  
100 at the University of Southern California who developed this strain (Cohen et al., 2013). More  
101 specifically, TgF344-AD rats were generated on a Fischer 344 background, bearing the Swedish mutant  
102 human amyloid precursor protein (APP<sup>swe</sup>) and  $\Delta$  exon 9 mutant human presenilin 1 (PSEN1 $\Delta$ E9)  
103 genes driven by the mouse prion promotor. TgF344-AD and WT were mated and heterozygous TG rats  
104 and WT littermates were obtained. WT and TgF344-AD littermates genotypes were determined from  
105 ear snips using real time PCR with specific probes designed for each transgene (Transnetyx, Cordova,  
106 TN). AD-related pathology in this rat model entails a moderate increase in levels of soluble amyloid  $\beta$ ,  
107 p-tau and gliosis from 6 months of age and increasing further with age. Also, an impaired entorhinal-  
108 hippocampal synaptic transmission is already present at this early age. This is followed by amyloid  $\beta$   
109 plaque formation, neurofibrillary tangles as well as neuronal loss and progressive synaptic and  
110 cognitive dysfunction (Bazzigaluppi et al., 2017; Cohen et al., 2013; Joo et al., 2017; Pentkowski et al.,  
111 2018; Rorabaugh et al., 2017; Smith and McMahon, 2018; Voorhees et al., 2017).

112 A total of 23 animals were used for longitudinal MR acquisitions, of which 7 WT and 8 TG animals were  
113 afterwards used for *ex vivo* analyses. An additional group of 10 WT and 9 TG rats were used for *ex vivo*  
114 analyses at 10 and 16 months of age. All animals were housed in a temperature- and humidity-  
115 controlled room on a 12-hour light-dark cycle with standard food and water available at libitum.

116

### 117 ***Animal handling***

118 A total of 23 female TgF344-AD rats (11 TG, 12 WT) was subjected to MRI procedures in a longitudinal  
119 manner at the ages of 6, 10, 12, 16 and 18 months (body weights, see Table S1). Two WT animals were  
120 excluded from the study as they developed a brain tumour. All imaging experiments were performed  
121 on spontaneously breathing rats under isoflurane (Isoflo<sup>®</sup>, Abbot Laboratories Ltd.) anaesthesia (5%  
122 for induction, 2% for set-up on the animal bed and maintenance), administered in a gaseous mixture  
123 of 30% O<sub>2</sub> and 70% N<sub>2</sub>. For the rsfMRI acquisition, a bolus of 0.05 mg/kg medetomidine (Domitor,  
124 Pfizer, Karlsruhe, Germany) was administered subcutaneously (s.c.) and 5 minutes afterwards,

125 isoflurane was reduced and kept at 0.4%. Continuous infusion of medetomidine was started 15  
126 minutes after bolus injection at a dose of 0.1 mg/kg/h to maintain the sedation level as it has been  
127 shown before that this anaesthesia regime is optimal for longitudinal resting state functional  
128 connectivity measurements (Grandjean et al., 2014a; Paasonen et al., 2018). After the rsfMRI  
129 procedures, isoflurane levels were gradually increased to make sure the animals remained stable for  
130 the DTI and 3D acquisition. After the MRI procedures, the effect of medetomidine was counteracted  
131 by injecting 0.1 mg/kg atipamezole (Antisedan, Pfizer, Karlsruhe, Germany) and animals were  
132 monitored closely until full recovery.

133 To immobilize the head in a reproducible flat-skull position during the MRI experiments, animals were  
134 secured in an MRI compatible rat stereotactic device. The head was held by a nose cone used for  
135 anaesthetic gas delivery, including tooth bar and blunt earplugs. An actively decoupled surface array  
136 (2x2) receiver coil was positioned on top of the head. Respiration rate, monitored with a small animal  
137 pressure pad (MR-compatible Small Animal Monitoring and Gating System, SA instruments, Inc.), was  
138 maintained within normal physiological ranges. Rectal temperature was maintained at  $(37.0\pm 0.5)$  °C  
139 using a feedback coupled warm air system (MR-compatible Small Animal Heating System, SA  
140 Instruments, Inc.). Blood oxygenation was monitored using a fibre optic pulse oximetry sensor (SA  
141 instruments, Inc.) positioned on the foot of the rats.

#### 142 143 ***Image acquisition***

144 Experiments were performed on a Bruker Pharmascan 7T imaging system (Bruker, Ettlingen,  
145 Germany). To ensure uniform slice positioning, 2D Turbo RARE T<sub>2</sub>-weighted images were acquired for  
146 each individual animal along three orthogonal directions to assess the subject's position (RARE; TR  
147 2500 ms; TE 33 ms; 10 slices of 1 mm; FOV (30 x 30) mm<sup>2</sup>; pixel dimensions (0.12 x 0.12) mm<sup>2</sup>). Field  
148 maps were acquired for each animal, followed by local shimming, which corrects for the measured  
149 inhomogeneity in a rectangular volume of interest (VOI) within the brain, covering the FOV of the DTI  
150 and rsfMRI. The timeline of the total experimental protocol with the different imaging modalities is  
151 illustrated in Fig. S1 A.



152 RsfMRI acquisition was performed using a 2D  $T_2^*$ -weighted single shot gradient echo (GE) echo planar  
153 imaging (EPI) sequence (2D GE-EPI; TR 2000 ms; TE 29 ms; 20 coronal slices of 0.7 mm, slice gap 0.1  
154 mm; 300 repetitions, frequency-encoding left-right). The field-of-view (FOV) was (30x30) mm<sup>2</sup> and the  
155 matrix size [128 x 128], resulting in voxel dimensions of (0.234 x 0.234 x 0.8) mm<sup>3</sup>. RsfMRI scans were  
156 acquired 40 minutes after the initial bolus administration and the total scan time was 10 minutes. The  
157 slice package covered a large part of the brain (Fig. S1 B) ranging from approximately Bregma 5.16 mm  
158 to Bregma -8.88 mm.

159 DTI scans were acquired using a two-shot spin echo (SE) EPI sequence (2D DW-SE-EPI; TR 7500 ms; TE  
160 26 ms; 20 coronal slices of 0.7 mm, slice gap 0.1 mm, b-value 800 s/mm<sup>2</sup>, diffusion gradient pulse  
161 duration  $\delta$  4 ms, diffusion gradient separation  $\Delta$  12 ms, frequency-encoding left-right), with diffusion  
162 sensitizing gradients applied along 60 optimally spread different directions. Fifteen  $b_0$  images were  
163 acquired ( $b=0$ s/mm<sup>2</sup>; 5  $b_0$  images per 20 diffusion weighted images) and the total acquisition time was  
164 approximately 20 minutes. The FOV was (30 x 30) mm<sup>2</sup> with a [128 x 128] acquisition matrix, resulting  
165 in a resolution of (0.234 x 0.234 x 0.8) mm<sup>3</sup>. The slice package was similar to the rsfMRI acquisition  
166 (Fig. S1B).

167 3D images were acquired using a 3D RARE sequence (TR 3185 ms; TE 44 ms; RARE factor 8; frequency-  
168 encoding head-foot). The matrix size was [256 x 64 x 50] and FOV (29 x 16 x 10.2) mm<sup>3</sup> resulting in a  
169 voxel resolution of (0.11 x 0.25 x 0.20) mm<sup>3</sup> with a total scan duration of 43 minutes.

170

### 171 ***rsfMRI data analysis***

172 Pre-processing of the rsfMRI data, including realignment, normalization and smoothing, was  
173 performed using SPM12 software (Statistical Parametric Mapping, <http://www.fil.ion.ucl.ac.uk>,  
174 (Hamaide et al., 2017; Jonckers et al., 2011)). First, all images within each session were realigned to  
175 the first image. This was done using a least-squares approach and a 6-parameter rigid body spatial  
176 transformation. Second, rsfMRI images were co-registered to the 3D RARE data of the same imaging  
177 session using a rigid body model with mutual information as the similarity metric. In parallel, the 3D

178 RARE data was spatially normalized to match a study-specific 3D-template, obtained in ANTs  
179 (Advanced Normalization Tools), using a global 12-parameter affine transformation followed by a  
180 nonlinear deformation protocol. Next, the transformation matrix of the spatial normalization was  
181 applied to the realigned and co-registered rsfMRI images while preserving the original voxel sizes.  
182 Afterwards, in-plane smoothing was done using a Gaussian kernel with full width at half maximum of  
183 twice the voxel size (FWHM = 0.468 mm x 0.468 mm). Finally, the Resting State fMRI Data Analysis  
184 toolbox (REST 1.8, <http://resting-fmri.sourceforge.net>) was used to filter the rsfMRI data. The filter  
185 was set between 0.01 and 0.1 Hz to rule out noise and low frequency drift and retain the low frequency  
186 fluctuations of the time course of the BOLD-signal that are of interest when performing FC studies.  
187 Independent Component Analysis (ICA) was performed on the rsfMRI data as described earlier  
188 (Jonckers et al., 2011) to determine which resting-state networks could be observed within the  
189 population examined using a design entailing all data sets (2 groups, 5 time points). Group ICA was  
190 performed using the GIFT-toolbox (Group ICA of fMRI toolbox, version 3.0a:  
191 <http://icatb.sourceforge.net/>). The number of components was set to 20. Anatomically relevant  
192 components were identified (Table 1, Fig. S2) based on a 3D anatomical template and with reference  
193 to the rat brain anatomical atlas (Paxinos and Watson, 2007). Components were named depending on  
194 the region where the peak intensity was observed.

195 The spatial maps derived from this data-driven analysis were then used to evaluate inter-regional and  
196 intra-regional FC. First, anatomically relevant ICA components were transformed into anatomical ROIs  
197 for further analysis. To assess the connectivity between regions, i.e. inter-regional FC, the average  
198 BOLD time course was extracted from each ROI for every individual scan. Next, correlation coefficients  
199 were calculated between the time courses of each pair of regions. These correlation coefficients were  
200 z-transformed, resulting in a correlation matrix. Mean z-transformed FC (zFC) matrices were  
201 calculated for each group.

202 Using the group-level ICA component spatial map as reference, seed regions of four voxels each were  
203 manually indicated in MriCron software at the peak intensity ( $T_{max}$ ) of the relevant component and

204 used to extract the respective temporal signal of each subject (14 seeds, see Table 1). This signal was  
205 then used to obtain the individual FC maps as described previously (Shah et al., 2016a). Briefly, the  
206 extracted temporal signal was compared to all other voxels within the brain, resulting in FC maps  
207 containing voxels significantly correlated with the given temporal signal. Intra-regional FC was  
208 calculated as the average correlation strength of all voxels within the corresponding group-level ICA  
209 component mask with the given seed.

210

### 211 ***DTI data analysis***

212 Pre-processing of the diffusion data was performed using SPM12 software as described previously  
213 (Hamaide et al., 2017). Briefly, images were realigned to correct for subject motion using the Diffusion  
214 II toolbox in SPM12. A rigid registration was performed between the  $b_0$  images, which was followed  
215 by an extended registration taking all DW images into account. Next, the realigned DW images were  
216 co-registered to the 3D RARE data set of the same imaging session and normalized to match the study-  
217 specific 3D template using the same procedure as the rsfMRI data. Then, the diffusion tensor was  
218 estimated and DTI parameter maps were computed, *i.e.* fractional anisotropy (FA), mean diffusivity  
219 (MD), axial diffusivity and radial diffusivity. Finally, all DTI parameter maps were smoothed in-plane  
220 using a Gaussian kernel with FWHM of twice the voxel size (FWHM = 0.468 mm × 0.468 mm). Next to  
221 a voxel-based analysis (VBA), a ROI-based analysis was performed by overlaying ROIs on the individual  
222 normalized maps and extracting the average DTI parameter value. Care was taken to ensure proper  
223 registration of the DTI parameter maps as well as correct positioning of each ROI. This additional ROI-  
224 based analysis was guided by the outcome of the rsfMRI data and included the cingulate, retrosplenial  
225 and hippocampal brain regions. Lastly, the entorhinal cortex was included to verify the obtained VBA  
226 results. ROIs were manually defined in AMIRA 5.4.0 software with the original corresponding ICA  
227 component, rat brain atlas (Paxinos and Watson, 2007) and an in-house rat brain ROI atlas as  
228 reference.

229

### 230 **3D RARE data analysis**

231 3D RARE data were analyzed using a ROI-based analysis and a tensor-based morphometry (TBM)  
232 analysis to assess local volume changes (Ashburner, 2015). Pre-processing of the 3D RARE data was  
233 performed in SPM12 software. A serial longitudinal registration (SLR in SPM12) was performed  
234 between the five individual 3D scans of an individual subject. Briefly, this step entailed the alignment  
235 of every scan to the intra-subject template using an intensity non-uniformity (bias field) correction  
236 followed by a rigid-body transformation and nonlinear registration steps (Ashburner and Ridgway,  
237 2012). During the SLR, the intra-subject template, or mid-point average corresponding to the 12  
238 month time point, was created and Jacobian determinants were obtained. These determinants  
239 describe the relative local shape difference, *i.e.* expansion ( $>1$ ) or contraction ( $<1$ ) of a voxel due to  
240 the non-rigid deformation compared to the template. Next, these Jacobian determinants were  
241 normalized to the study-specific 3D template using a similar procedure as described above in order to  
242 perform voxel-based analyses. During this step, Jacobian determinants were modulated to preserve  
243 relative volume differences existing between different subjects. A final step included in-plane  
244 smoothing using a Gaussian kernel with FWHM of twice the voxel size ( $0.22 \times 0.50$ ) mm<sup>2</sup>.  
245 Additionally, the study-specific 3D template was used by the FMRIB Automated Segmentation Tool  
246 (FAST; (Zhang et al., 2001)) embedded in FSL, to extract tissue probability maps reflecting mainly grey  
247 matter, white matter and cerebrospinal fluid. The three probability maps created in this step were  
248 used as tissue class *priors* for segmenting the individual midpoint averages in SPM12. In parallel, a  
249 whole brain mask for the 3D template as well as a hippocampal ROI were manually delineated in Amira  
250 5.4.0 software. After back projection of the 3D template whole brain mask as well as the hippocampal  
251 ROI and midpoint average tissue segments to the individual scans in native space, volumes were  
252 extracted for whole brain, grey matter (GM), white matter (WM), cerebrospinal fluid (CSF) and  
253 hippocampus. Relative volumes were calculated by dividing the tissue volumes by the absolute whole  
254 brain volume.

255

256 ***Ex vivo Pathology***

257 At the ages of 10 (N<sub>WT</sub>=6; N<sub>TG</sub>=5), 16 (N<sub>WT</sub>=4; N<sub>TG</sub>=4) and 18-20 months (N<sub>WT</sub>=7; N<sub>TG</sub>=8), brain tissue  
258 samples were acquired for *ex vivo* pathology analyses. Following transcardial perfusion with 0.9%  
259 NaCl, brains were dissected and fixed by immersion in 0.1 M phosphate buffered 4%  
260 paraformaldehyde pH 7.4 for 4 hours. After washing with PBS, brains were transferred in 0.1 M  
261 phosphate buffered 30% sucrose solution pH 7.4 at 4 °C for at least 48h. Brains were then cut in 40  
262 µm sagittal sections using a sliding microtome (Leica) on dry ice and sections were serially collected  
263 into 10 tubes containing cryoprotectant solution (25% v/v glycerol, 0.05 M sodium phosphate buffer  
264 pH 7.4, 25% v/v ethylene glycol), each tube containing 1/10 of a hemisphere with 400 µm inter-section  
265 separation. Series were thereafter stored at -20 °C until processing.

266 Following antigen-retrieval with citrate buffer pH 6.0 (Sigma-Aldrich, C9999) for 1 min at 100°C,  
267 fluorescent immunohistological labelling was performed as previously described (Adamczak et al.,  
268 2017). Primary antibodies: mouse anti-Amyloid beta (Covance, SIG-39300) 1:500; rabbit anti-Iba1  
269 (Abcam, ab178846) 1:1000; guinea-pig anti-GFAP (Progen, GP52) 1:500; guinea-pig anti-NeuN  
270 (Millipore, MAB377) 1:500. Secondary antibodies: donkey anti-mouse Alexa 488nm (Invitrogen,  
271 A21202) 1:1000, donkey anti-rabbit Alexa 568nm (Invitrogen, A10042) 1:1000, donkey anti-guinea-pig  
272 Alexa 647nm (Jackson, 706-605-178) 1:1000. Nuclei were counterstained with DAPI (Sigma-Aldrich,  
273 D9564, 0.5 µg/mL). For quantification, fluorescence images were acquired using an Olympus VS120  
274 Slide Scanner and the rat brain atlas from Paxinos and Watson (Paxinos and Watson, 2007) was used  
275 as reference to localize the regions of interest (one micrograph per region of interest and rat).  
276 Micrographs were further processed with ImageJ Software 1.46r (National Institutes of Health) and  
277 FIJI based on ImageJ 1.50a (Schindelin et al., 2012). Microglia (Iba1<sup>+</sup> cells) were manually counted. The  
278 percentages of area covered by beta-amyloid, GFAP or NeuN were determined in the regions of  
279 interest following binarization with fixed detection threshold slightly above background intensity for  
280 each marker and age-group. High resolution micrographs for illustration purposes (Fig S9) were  
281 acquired with a Zeiss LSM710 confocal microscope.

282

283 ***Statistical analyses***

284 Voxel-based statistical analyses of FC maps, DTI parameter maps and Jacobian determinants of the 3D  
285 anatomical scans were performed in SPM12 software, where a repeated measures two-way ANOVA  
286 design was used to test for the interaction between age and genotype as well as for the main effect  
287 of age or genotype. For this, a 2x2 factorial design was constructed with genotype (TG, WT) as  
288 between-subject factor and age (6, 10, 12, 16 and 18 months) as within-subject factor. To account for  
289 errors induced by multiple comparisons, a family wise error (FWE) correction was applied with  
290  $p_{FWE} < 0.05$  and a minimum cluster size of 10 voxels ( $k > 10$ ). Besides this very stringent correction, all  
291 statistical maps were assessed with a more liberal false discovery rate (FDR) correction ( $p < 0.05$ ) and  
292 a minimum cluster size of 10 voxels. All statistical voxel-based maps are shown overlaid on an  
293 anatomical 3D study-specific template (displayed FDR  $p < 0.05$ ; minimum 10 voxels). Results are  
294 reported by the highest voxel  $F_{max}$  or  $T_{max}$  value and the associated voxel  $p_{FWE}$  and  $p_{FDR}$  value (peak-  
295 level  $p$ ). In case a significant interaction [age x genotype] effect or main effect of age or genotype was  
296 found according to the voxel-based analysis, data within these clusters were extracted from each  
297 individual scan and plotted in a graph for further examination.

298 All ROI-based analyses (rsfMRI, DTI and 3D) as well as the differences between body weights of the  
299 animals were assessed using a repeated measures two-way ANOVA in Graphpad Prism 6.0 or Matlab  
300 to test for the interaction between age and genotype as well as for the main effect of age or genotype.  
301 *Post hoc* tests were performed using Sidak's multiple comparisons test with  $p < 0.05$ . In case multiple  
302 analyses were performed in parallel, a false discovery rate (FDR) correction ( $p < 0.05$ ) was applied to  
303 account for the multiple testing.

304 *Ex vivo* data were analyzed in Graphpad Prism 6.0 where a two-way ANOVA design was used to test  
305 for the interaction between age and genotype as well as for the main effect of age or genotype. *Post*  
306 *hoc* Sidak's multiple comparisons tests were applied with  $p < 0.05$ . For the analysis of the amyloid

307 plaque load in the TgF344-AD rats, a one-way ANOVA with Tukey's *post hoc* tests ( $p < 0.05$ ) was used  
308 to assess the age-dependent effect.

309 All results are shown as mean  $\pm$  SEM (standard error of mean). When no significant [age x genotype]  
310 interaction was found, only main effects for age and genotype are reported.

311

## 312 **RESULTS**

### 313 ***Reduced functional connectivity between brain regions***

314 A group ICA analysis was performed using a pre-set of 20 components, of which 14 were classified to  
315 be anatomically relevant (Fig. S2). The selected components could be identified as cortical networks,  
316 *i.e.* sensorimotor cortical components or cingulate and retrosplenial components, and subcortical  
317 networks. Other, irrelevant, components included noise and blood vessel artifacts. Based on the  
318 regions obtained from this ICA outcome, an inter-regional FC analysis was performed to assess the  
319 functional connectivity between the different regions ~~networks~~ at every time point (Fig. 1). As no  
320 significant [age x genotype] interaction survived the FDR correction, only main effects are reported. A  
321 significant genotype effect indicating widespread decreased FC in TG rats compared to WT rats was  
322 found for almost all connections. CPU, S1<sub>HL-FL</sub> and S1<sub>ULP</sub>-S2 regions did not show any significantly altered  
323 connections with any other region (Fig. 1 F). An examination of the overall (whole brain) average inter-  
324 regional FC at every time point confirmed that TG rats had consistently reduced FC values compared  
325 to WT ( $F_{1,18} = 20.62$ ,  $p = 0.0003$ ), with the largest difference occurring at 10 months of age (-17%).

326

327 To further elucidate how this decreased FC in TG animals evolved along disease progression,  
328 connections displaying a main effect of genotype were examined in more detail. This revealed only  
329 decreased FC in TG rats as compared to WT, without signs of significantly increased FC in the TG group  
330 (Fig. 1 G, Fig. S3). As early as 6 months of age, slightly decreased FC values were present in TG rats for  
331 several connections with the hippocampus, cingulate and retrosplenial cortices, and sensorimotor  
332 regions. This effect progressed towards an overall severely reduced FC at the age of 10 months, with

333 most connections showing a strong significant decrease in TG animals compared to WT. This reduced  
334 FC in TG rats persisted at later time points, although somewhat less pronounced throughout the brain.  
335 Important to note is that connections between typical brain regions involved in AD, such as the  
336 cingulate, retrosplenial and hippocampal regions, were decreased in TG animals starting at 10 months.  
337 Especially connections between hippocampal, cingulate and retrosplenial regions showed an age-  
338 dependent increasing difference between WT and TG animals. Beside the genotype differences, slight  
339 age-dependent alterations were present in both groups (Fig. 1 F) for connections with the CPU and M1  
340 regions, reflecting an age-dependent FC reduction. In contrast, FC between V2<sub>MM-ML</sub>/V1-HC and Au<sub>D-  
341 v</sub>/Au1-HC displayed a significant increase when comparing young (6-10 months) and older (16-18  
342 months) ages.

343

344 Because the largest FC differences were observed at 10 months of age, which then slightly diminished  
345 towards 16 months of age, an additional examination of age-dependent effects in these time intervals  
346 was performed. More specifically, the average monthly change of FC was computed for the time  
347 intervals between 6 and 10 months of age as well as between 10 and 16 months of age for both TG  
348 and WT animals. It can be appreciated from Fig. S4 that a differential effect was present for each  
349 genotype. As such, WT animals displayed an overall strengthening of FC between 6 and 10 months,  
350 whereas TG FC values remained fairly low (Fig. S4 A). In contrast, an age-dependent strengthening of  
351 FC in TG animals only occurred between 10 and 16 months of age (Fig. S4 B). In this time interval, WT  
352 animals showed a further strengthening of several connections with HC, V2<sub>MM-ML</sub>/V1 and Au<sub>D-v</sub>/Au1  
353 regions. Although no significant interaction effects of [genotype x time interval] survived the FDR  
354 correction, it can still be appreciated that this seemingly opposite effect was most pronounced in the  
355 following connections: S1<sub>BF</sub>-Cg1/RS ( $F_{1,18}=11.5$ ;  $p=0.07$ ); S1<sub>TrL</sub>-RSG ( $F_{1,18}=11.6$ ;  $p=0.07$ ); V2<sub>MM-ML</sub>/V1-  
356 RSG ( $F_{1,18}=11.4$ ;  $p=0.07$ ); S1<sub>TrL</sub>-Cg1/RS ( $F_{1,18}=10.2$ ;  $p=0.08$ ); Au<sub>D-v</sub>/Au1-RSG ( $F_{1,18}=9.15$ ;  $p=0.09$ ).

357

358 ***Reduced local functional connectivity***



359 To assess the functional connectivity within a certain ~~component or region~~, the individual temporal  
360 BOLD signal was extracted from the relevant ~~component~~ seed and used to calculate intra-regional FC  
361 (Fig. S5). Consistent with the inter-regional analysis, lower FC values were present in the TG group  
362 compared to WT in auditory regions ( $F_{1,18}=13.13$ ;  $p=0.0067$ ), cingulate/retrosplenial cortex  
363 ( $F_{1,18}=13.69$ ;  $p=0.0067$ ), frontal cingulate cortex ( $F_{1,18}=21.02$ ;  $p=0.0021$ ), hippocampus ( $F_{1,18}=6.64$ ;  
364  $p=0.038$ ), retrosplenial cortex ( $F_{1,18}=10.35$ ;  $p=0.0134$ ), the right S1<sub>Tr</sub> region ( $F_{1,18}=7.38$ ;  $p=0.0329$ ) and  
365 the visual cortices ( $F_{1,18}=19.65$ ;  $p=0.0021$ ). Furthermore, an age-dependent increase of FC was present  
366 in both groups for the motor ( $F_{4,72}=4.00$ ;  $p=0.0252$ ), retrosplenial regions ( $F_{4,72}=3.80$ ;  $p=0.0259$ ), visual  
367 ( $F_{4,72}=4.33$ ;  $p=0.0238$ ) and auditory cortices ( $F_{4,72}=6.24$ ;  $p=0.0028$ ). This age-dependent change was  
368 already evident in WT animals between 6 and 12-18 months, whereas TG animals only displayed an  
369 age-dependent increase after 10 months of age.

370

371 As the strongest local (*i.e.* intra-regional ~~within-component~~) reduction of FC was found for the frontal  
372 cingulate cortex (Cg2), an illustration of localized genotype differences of the ~~within-component~~ intra-  
373 regional FC, by means of a seed-based analysis, is shown in Fig. 2 for this region. A significantly reduced  
374 FC was present in TG animals compared to WT animals (Fig. 2 A;  $p_{FWE}<0.0001$ ;  $p_{FDR}<0.001$ ; 976 voxels;  
375  $F_{max}=46.01$ ). Also an age-dependent alteration of FC was present in a cluster of 352 voxels  
376 ( $p_{FWE}<0.0001$ ;  $p_{FDR}<0.001$ ;  $F_{max}=12.85$ ; Fig. 2 B). When plotting the corresponding FC values (Fig. 2 C),  
377 the strongest difference between TG and WT rats was present at 10 months of age. TG animals  
378 presented a minor increase of FC between 10 and 16 months of age, resulting in slightly smaller  
379 genotype differences at later ages. Note that these results differ slightly as compared with Fig. S5,  
380 when taking into account the entire region-rather than only the localized significant genotype effect  
381 as presented in Fig. 2.

382

383 ***Progressive microstructural alterations***

384 To evaluate whether microstructural changes could be observed in TG rats, a voxel-based analysis of  
385 the DTI parameter maps was performed. As illustrated in Fig. 3 and Table S2, several clusters were  
386 found to be significantly altered in TG animals compared to WT, for both FA and MD.

387 More specifically, decreased MD values were present in the ventricular regions of the TG animals,  
388 whereas MD was significantly elevated in the primary motor and somatosensory cortex (Fig. 3 A; Table  
389 S2). When lowering the threshold from a stringent FWE-corrected to FDR-corrected  $p < 0.05$ , an  
390 additional cluster in the subgeniculate nucleus appeared, with higher MD values in TG animals  
391 compared to the WT group. An age-dependent decline of MD for both groups was found in clusters in  
392 the striatum, internal capsule, corpus callosum, and part of the external capsule (Fig. S6 A). Between  
393 6 and 10 months of age, the strongest reduction was observed for both groups, which was followed  
394 by a minor reduction between 12 and 18 months of age mainly in WT animals (data not shown).

395

396 An investigation of FA (Fig. 3 B; Table S2) revealed that TG animals had strongly decreased FA values  
397 in a large bilateral cluster comprised of the ventral part of the external capsule stretching into the  
398 entorhinal cortex. TG rats showed a progressive decrease of FA within this region starting at 10 months  
399 of age leading up to a 10% decrease at 18M of age compared to WT. Importantly, a ROI-based analysis  
400 of the full entorhinal cortex confirmed this result showing a similar age-dependent progressive  
401 decrease of FA (data not shown), which is in agreement with previous studies showing early AD  
402 pathology in this brain region (Rorabaugh et al., 2017). When lowering the threshold from a stringent  
403 FWE-corrected to a more exploratory FDR-corrected  $p < 0.05$ , additional bilateral cortical clusters were  
404 found, located in the motor (M1) and somatosensory ( $S1_{BF}$ ,  $S1_{HL-FL}$ ) cortex. Again, lower FA values were  
405 present in TG animals as compared to WT animals. In contrast, increased FA values were present in a  
406 cluster comprising the corpus callosum and dorsal part of the external capsule. Also, a small section  
407 of the lateral somatosensory cortex ( $S2$ ,  $S1_{ULp}$ ) showed higher FA in TG animals compared to WT.  
408 Age-dependent alterations of FA were present in both groups in bilateral cortical clusters, as well as  
409 in the cingulum (Fig. S6 B). *Post hoc* tests within these main effects, revealed that an age-dependent

410 decline of FA in these regions started between 6 and 10 months for the cortical regions and between  
411 12 and 16 months for the cingulum (data not shown). Importantly, age-dependent alterations were  
412 again most pronounced in the WT animals.

413

414 Axial and radial diffusivity measures also differed between WT and TG animals (data not shown). As  
415 such, both axial and radial diffusivity values were significantly lower in TG rats in the ventricular area  
416 and elevated in cortical areas, similar to changes of MD. Additionally, axial diffusivity was significantly  
417 lower in the ventral part of the external capsule and increased in the corpus callosum, similar to FA.  
418 In line with age-dependent changes of FA and MD, respectively, age-dependent alterations of axial  
419 diffusivity were present in the cingulum and anterior cingulate cortex, corpus callosum and the  
420 external capsule, whereas radial diffusivity showed an age-dependent attenuation in the caudate  
421 putamen.

422

423 An additional ROI-based analysis (Fig. 4) was performed to further examine regions characteristically  
424 involved in AD, *i.e.* the cingulate regions and hippocampus (Weston et al., 2015). Importantly, these  
425 regions were also identified to be affected in the rsfMRI data. The cingulate and hippocampal ROIs  
426 were similar to the rsfMRI analysis to identify potential co-existing functional and structural alterations  
427 as FC in these regions was found to be severely affected. As described before, TG animals had  
428 significantly lower FC both within and between the Cg2 and Cg1RS regions. The corresponding DTI  
429 parameters showed a significant interaction effect of [age x genotype] for FA (Cg2:  $F_{4,64}=3.043$ ;  
430  $p=0.0233$ ; Cg1RS:  $F_{4,64}=3.873$ ;  $p=0.007$ ). *Post hoc* tests indicated that for both regions TG and WT  
431 animals differed most at more advanced ages. In the Cg2 region (Fig. 4 A), this effect was due to an  
432 age-dependent decline of FA in the TG group (-3% between 6M and 16M,  $p=0.0069$ ; -4% between 6M  
433 and 18M;  $p=0.0005$ ), whereas WT values remained stable over time. In contrast, although WT animals  
434 presented an age-dependent increase of FA in the Cg1RS region (+4% between 6M and 16M;  
435  $p=0.0156$ ), no change was present for the TG group leading to a difference between both groups of

436 5% at this advanced stage (Fig. 4 B). This coincided with significantly increased MD ( $F_{1,18}=8.519$ ;  
437  $p=0.0092$ ) and RD values ( $F_{1,17}=12.02$ ;  $p=0.003$ ) in the Cg1RS region of TG animals. In the hippocampus,  
438 significantly lower FC co-existed with decreased FA values ( $F_{1,16}=9.949$ ;  $p=0.0061$ ) in TG animals (Fig.  
439 4 C). It can be appreciated from the graph that this decreased FA in TG animals was aggravated at  
440 more advanced age due to a minor (non-significant) decrease of -2.5% in TG animals at 18 months  
441 compared to 6 months. Important to note is that whereas these regions did not appear in the VBA  
442 (Fig. 3), clusters within these regions were still observed when lowering the threshold further to an  
443 uncorrected p-value  $p<0.05$  (data not shown) corroborating this ROI-based analysis.

444

#### 445 ***Macroscopic alterations***

446 First, a ROI-based analysis of the whole-brain volume was performed to identify global differences  
447 between both groups (Table S3). This analysis revealed a strong trend for enlarged whole brain  
448 volumes in TG animals ( $F_{1,18}=3.571$ ;  $p=0.075$ ; +2%) throughout the entire experiment. Additionally, an  
449 age-dependent increase of whole brain volumes was present in both groups ( $F_{4,72}=18.55$ ;  $p<0.0001$ )  
450 as can be appreciated in Table S3. An examination of the relative volumes of grey matter, white  
451 matter, cerebrospinal fluid and hippocampal region revealed no significant difference (data not  
452 shown).

453 Next, a TBM analysis was performed to identify localized macrostructural differences (Fig. S7). Here,  
454 we used modulated Jacobian determinants corrected for the initial whole brain volume difference to  
455 account for the pre-existing volume difference between both groups. This TBM analysis indicated a  
456 differential genotype effect depending on the region investigated which was consistent throughout  
457 all ages investigated, indicating a potential transgenic developmental effect rather than a pathology-  
458 induced difference (Fig. S7 A). WT animals showed increased Jacobian values in frontal GM regions  
459 ( $p_{FWE}=0.001$ ;  $p_{FDR}=0.003$ ;  $k=7863$ ;  $T_{max}=5.55$ ) as well as in a cluster comprising the raphe nuclei,  
460 mesencephalic reticular formation and part of the cerebral peduncle ( $p_{FWE}<0.001$ ;  $p_{FDR}<0.001$ ;  $k=5108$ ;  
461  $T_{max}=8.90$ ). This reflects slightly larger regional volumes compared to TG animals. In contrast, TG

462 animals had larger relative volumes in the hypothalamic regions ( $p_{FWE}=0.002$ ;  $p_{FDR}=0.0.03$ ;  $k=8145$ ;  
463  $T_{max}=5.31$ ), posterior cortical regions, including the retrosplenial cortex ( $p_{FWE}=0.001$ ;  $p_{FDR}=0.002$ ;  
464  $k=15132$ ;  $T_{max}=5.61$ ) as well as bilateral clusters in the primary sensorimotor cortex ( $p_{FWE}=0.001$ ;  
465  $p_{FDR}=0.002$ ;  $k=4211$ ;  $T_{max}=5.56$ ). Beside these persistent genotype differences, similar age-dependent  
466 changes were detected in both groups (Fig. S7 B) which were slightly more pronounced in the WT  
467 group. No age-dependent genotype-specific changes were present indicative of potential cortical  
468 atrophy or ventricular enlargement in the TgF344-AD group.

469

#### 470 ***Ex vivo AD pathology***

471 Microglia density, based on the detection of Iba1<sup>+</sup> expression, was calculated for the hippocampus,  
472 entorhinal cortex, cingulate cortex, somatosensory cortex and thalamus (Fig. 5, 6). The highest density  
473 of microglia was observed in the hippocampus regardless of the genotype. However, as early as 10  
474 months of age, a significantly higher microglia density could be detected in TG rats compared to the  
475 WT group, within the hippocampal molecular layer ( $F_{1,28}=20.69$ ;  $p<0.0001$ ;  $p_{10M}=0.022$ ) and in the hilus  
476 ( $F_{1,28}=94.59$ ;  $p<0.0001$ ;  $p_{10M}=0.0384$ , Fig. 5 A, Fig. 6 D-F). At 16 and 20 months of age, the density of  
477 Iba1-expressing cells in the hilus further increased in TG rats and was highly significantly different as  
478 compared to the WT-type group ( $p_{16M}<0.0001$ ;  $p_{20M}<0.0001$ ). At this time point, the morphology of  
479 the microglia was characteristic of the so-called activated microglia and were often positive for  
480 amyloid  $\beta$  as a result of their phagocytic activity. Finally, in the 20 month old TG rats, the density of  
481 microglia detected in the entorhinal cortex was also higher as compared to the wild-type group  
482 ( $F_{1,26}=14.32$ ;  $p=0.008$ ;  $p_{20M}=0.0187$ ).

483 Accumulation of amyloid plaques was observed in the hippocampus, cingulate cortex, somatosensory  
484 cortex and thalamus as expected also from the MRI measurements (Fig. 5 B). In contrast, the striatum  
485 which showed no functional or microstructural deficits, did not accumulate amyloid plaques, but  
486 striatal microglia showed morphological signs of mild activation (Fig. 6 J-L). Again, the hilus contained  
487 the highest deposition of plaques (Fig. 5 B, Fig. 6 A-F) and these significantly increased until 20 months

488 of age ( $F_{2,14}=5.124$ ;  $p=0.0396$ ). In the molecular layer of the hippocampus, a significant increase in  
489 amyloid plaques took place between 10 and 16 months ( $F_{2,14}=5.032$ ;  $p=0.0396$ ). Although less  
490 abundant, the amyloid plaque deposition also significantly increased over time in the cingulate cortex  
491 ( $F_{2,33}=3.460$ ;  $p=0.05$ ; Fig. 6 A-C, G-I), somatosensory cortex ( $F_{2,16}=5.407$ ;  $p=0.0396$ ) and in the thalamus  
492 ( $F_{2,17}=8.552$ ;  $p=0.0189$ ). Additionally, amyloid  $\beta$  positive staining could be observed in blood vessels of  
493 TG animals at all ages investigated, whereas this effect was not found in WT animals (Fig. 7 C-D).  
494 Moreover abundant amyloid  $\beta$  could be detected in the choroid plexus of the 20 month transgenic  
495 animals (Fig. 6 C).  
496 No significant changes in GFAP or NeuN expression could be detected between age-matched TG and  
497 WT animals (data not shown). Nevertheless, neurotoxicity of amyloid plaques could be observed, as  
498 the density of NeuN-expressing neurons in the vicinity of the plaques, for example in the  
499 somatosensory cortex, was scarce (Fig. 7 A-B). However, this neuronal loss was very local to the  
500 plaques and not large enough to be detectable within larger regions of analysis.

501

## 502 **DISCUSSION**

503 Preclinical studies are of utmost importance to improve our knowledge of the underlying mechanisms  
504 of AD and therefore allowing improved early detection of the disease. However, until now most  
505 studies have focused on the examination of transgenic mouse models which usually present only one  
506 aspect of the disease thus limiting the translational value of these studies. Here, we present the first  
507 longitudinal *in vivo* MRI characterization of the TgF344-AD rat model exhibiting all hallmarks of human  
508 AD. Using the highly translational methods of rsfMRI and DTI, we have shown that TgF344-AD rats  
509 display severely diminished FC at early stages of the disease and that this is followed by progressive  
510 microstructural alterations.

511

512 ***Reduced functional connectivity precedes microstructural alterations in the TgF344-AD rat***

513 In the present study, we have shown that already at an early stage, *i.e.* six months of age, minor  
514 functional deficits could be detected in the absence of microstructural alterations. This included  
515 impaired connectivity with the hippocampus, cingulate and sensory regions. At this age, TgF344-AD  
516 rats have been previously described to exhibit only low levels of pathological AD characteristics,  
517 including elevated concentrations of soluble A $\beta$ , some reactive gliosis and tau hyperphosphorylation,  
518 as well as enhanced anxiety-like behaviour (Cohen et al., 2013; Pentkowski et al., 2018; Rorabaugh et  
519 al., 2017). Although this early phase of the disease is characterized by only minor pathological  
520 hallmarks, the initial rise of A $\beta$  could already lead to synaptic dysfunction resulting in the observed FC  
521 alterations (Mucke and Selkoe, 2012; Selkoe, 2002; Shah et al., 2016a; Smith and McMahon, 2018).  
522 The existence of functional hypoconnectivity is in agreement with other rodent and human AD studies,  
523 both before and after plaque deposition (Badhwar et al., 2017; Balachandar et al., 2015; Grandjean et  
524 al., 2014b). Interestingly, Muñoz-Moreno and colleagues recently used a connectomics approach to  
525 evaluate functional and structural network properties in 5 month old male TgF344-AD rats. They  
526 reported that early learning and memory deficits in this model are linked with a slightly altered brain  
527 functional and structural organisation in regions such as the retrosplenial cortex, entorhinal cortex,  
528 amygdala and hippocampus (Munoz-Moreno et al., 2018). Although the animals in that study were  
529 cognitively trained before FC assessment, which could alter the FC readout (Nasrallah et al., 2016),  
530 these results further support our early FC dysfunction.

531 In contrast, also hypersynchronous FC has been observed before A $\beta$  deposition in early stages of AD  
532 (Quiroz et al., 2015; Shah et al., 2016a). This discrepancy might possibly be explained by differences  
533 in timing of FC assessment. As such, hypersynchronous FC could have occurred even before the age  
534 of 6 months in the TgF344-AD rat model. It is further important to note that based on the results  
535 presented in our study, it is not possible to rule out a potential developmental effect in this rat model  
536 of AD due to exposure to the transgenic proteins at early postnatal stages which could affect early  
537 brain functional as well as structural development. Future studies could explore brain development in  
538 this rat model in more detail to verify this hypothesis.

539

540 Consistent with previous reports of neurovascular dysfunction (Bazzigaluppi et al., 2017; Joo et al.,  
541 2017), we have identified severely reduced functional connectivity throughout the brain of TG rats at  
542 the age of 10 months. Interestingly, this occurred at an age at which still only few pathological  
543 hallmarks are present in this rat, as shown by our *ex vivo* analyses as well as others (Bazzigaluppi et  
544 al., 2017; Joo et al., 2017; Rorabaugh et al., 2017). Of specific interest are the cingulate cortex and  
545 hippocampus, two brain regions classically associated with AD pathology in humans (Selkoe, 2001)  
546 and in which strong AD pathology is present in TgF344-AD rats. A severely decreased FC was present  
547 both within the regions and with other brain regions, preceding a reduction of FA in these respective  
548 brain areas. As described above, initial FC deficits in the absence of clear structural damage are  
549 thought to occur due to synaptic alterations (Mucke and Selkoe, 2012). Importantly, BOLD FC  
550 measures have a dual vascular and neuronal origin, so vascular dysfunction should also be taken into  
551 account (Peca et al., 2013; Princz-Kranz et al., 2010). In line with this, we observed amyloid  $\beta$  positive  
552 blood vessels in TG animals across all ages investigated, which agrees with previous data as well.  
553 Cohen *et al.* presented progressive age-dependent cerebral amyloid angiopathy in 16 and 26 month  
554 old animals (Cohen et al., 2013). In addition, Joo and colleagues (Joo et al., 2017) showed that even at  
555 the age of 9 months, a significant amount of A $\beta$  deposits was present in cortical arterioles.  
556 Importantly, they described that loss of vascular contractility at 9 months of age coincided with severe  
557 neuronal network dysfunction, as assessed with electrophysiological techniques (Bazzigaluppi et al.,  
558 2017; Joo et al., 2017). TgF344-AD rats exhibited decreased neuronal network functioning in the  
559 somatosensory cortex, cingulate cortex and hippocampus (Bazzigaluppi et al., 2017; Joo et al., 2017).  
560 Moreover, they had a decreased low-gamma resting power in both hippocampus and cingulate region  
561 as well as a reduced connectivity between both regions (Bazzigaluppi et al., 2017; Joo et al., 2017).  
562 Since there is a strong link between electrophysiological measures and BOLD FC measures (Scholvinck  
563 et al., 2010; Weaver et al., 2016), these findings of neuronal network dysfunction are in good



564 agreement with our data showing reduced BOLD-based FC both within and between various brain  
565 regions.

566 Results presented in this study indicate an overall reduced FC in TG rats compared to WT across all  
567 ages investigated (*i.e.* significant main genotype effects), despite progressive AD pathology.  
568 Nevertheless, the strongest effect was present at 10 months of age, with connections throughout the  
569 entire brain showing a loss of FC compared to age-matched WT. Most connections followed a pattern  
570 of no or slightly reduced FC at 6 months, followed by strongly reduced FC at 10 months and slightly  
571 dampened, but still significant, hypoconnectivity at more advanced ages. This pattern is likely due to  
572 differential age-dependent alterations of FC in both genotypes (Fig. S4). More specifically, WT animals  
573 presented an age-dependent strengthening of FC between 6 and 10 months of age, whereas TG  
574 animals only showed such strengthening between 10 and 16 months of age.

575 Of particular interest is the connectivity between hippocampal and cingulate cortical regions, as this  
576 connection displayed a different pattern of FC dysfunction. In the present study, no attenuation of this  
577 interaction was found at 6 months of age, however, an age-dependent increasing difference was  
578 present between WT and TG ranging from a 10% (non-significant) decrease at 6 months to almost 20%  
579 at 18 months. Interestingly, disturbances of this interaction have been linked to cognitive deficits in  
580 several neuropsychiatric disorders, including AD (Arenaza-Urquijo et al., 2013; Gordon, 2011; Leech  
581 and Sharp, 2014; Sampath et al., 2017; Sigurdsson and Duvarci, 2015). This finding could prove to be  
582 a valuable *in vivo* marker of pathology in this model, *e.g.* when evaluating new treatment options.

583

#### 584 ***Progressive microstructural deficits in the TgF344-AD rat***

585 In contrast to the functional data, no or only minor alterations of the microstructural integrity were  
586 present in 6 and 10 month old TgF344-AD rats. At 10 months of age, only small unilateral clusters in  
587 the frontoparietal somatosensory cortex and the external capsule/entorhinal cortex presented a  
588 slightly attenuated MD or FA, respectively. These changes were aggravated in advanced stages of the  
589 disease, with large bilateral clusters of increased MD and decreased FA at 18 months. An additional

590 ROI-based analysis further revealed age-dependent alterations in FA of the hippocampus and  
591 cingulate cortices. This progressive and age-dependent degenerative pattern seems in line with the *ex*  
592 *vivo* AD pathology in this rat model as shown by us and others (Cohen et al., 2013; Rorabaugh et al.,  
593 2017), including progressive amyloid plaque load in various regions and increasing microgliosis in the  
594 hippocampus. The histopathology as described here is in good agreement with previous reports of AD  
595 pathology in this model (Bazzigaluppi et al., 2017; Cohen et al., 2013; Joo et al., 2017) and could affect  
596 the tissue organisation leading to altered diffusion measurements. More specifically, pathology in this  
597 rat model was reflected by increased mean diffusivity and decreased anisotropy, which is thought to  
598 represent microstructural cellular damage, alterations in tissue organisation, breakdown of diffusion  
599 barriers and eventually neuronal loss (Stebbins and Murphy, 2009; Weston et al., 2015). Indeed, a  
600 previous *ex vivo* diffusion weighted imaging study in this rat model presented dystrophic neurites in  
601 the hippocampus, characterized by enlarged axons and vacuolar pathology, concomitant with age-  
602 dependent decreased anisotropy measures (Daianu et al., 2015). Although they used only one animal  
603 per age and performed *ex vivo* measurements, these results do support the *in vivo* data as presented  
604 here.

605 Interestingly, according to our VBA DTI data, alterations of MD were most prominent in the sensory  
606 cortex in TG animals. Though we could not quantify actual neuronal loss based on the NeuN staining  
607 in this region, we did observe a NeuN vacuum around the amyloid plaques. It is possible that NeuN  
608 positive dying neurons were phagocytized by microglia, thus complicating the quantification  
609 (Voorhees et al., 2017) or that neuronal loss was not yet extensive enough to detect using this method.  
610 Nevertheless, neuronal loss has been previously observed in TG rats in cortical and hippocampal  
611 regions starting at 16 months of age (Cohen et al., 2013; Voorhees et al., 2017). It has further been  
612 suggested that in familial AD an initial decreased MD is present in the presymptomatic phase due to  
613 cellular hypertrophy and inflammation (Weston et al., 2015), however, we did not observe this in our  
614 study. Future studies could elucidate whether this effect can be detected in this model before the age  
615 of 6 months. Alternatively, larger group sizes or different methodologies could prove to be more

616 sensitive to these early changes. Similarly, though it might be hypothesized that MD values decrease  
617 at more advanced stages due to cortical thinning, this effect was not observed in the present study.  
618 In line with this, the morphometric analysis of the 3D anatomical scans did not reveal significant  
619 volume loss typical of AD, *i.e.* cortical or hippocampal atrophy and ventricular enlargement. A possible  
620 explanation is that the present study evaluated TgF344-AD rats only up to the age of 18 months,  
621 whereas neuronal loss is more extensive at 26 months (Cohen et al., 2013). It is therefore possible  
622 that the methods used in our study were not sensitive enough to already detect actual neuronal loss  
623 at 18 months or that neuronal loss is not yet that pronounced at this age.

624

625 In contrast to the evolution of functional connectivity over time in each group, we observed similar  
626 micro-and macrostructural changes between 6 and 10 months in both groups. Only thereafter a slight  
627 discrepancy was present between age-related alterations in WT and TG animals, with less pronounced  
628 or no changes in the TG group. Again, this corroborates the fact that the early pathological features of  
629 AD (mainly soluble amyloid  $\beta$ ) affect the functional organisation of the brain prior to structural aspects.  
630 It is further likely that the increase of FC between 10 and 16 months is driven by pathological (Shah et  
631 al., 2016b) or perhaps compensatory mechanisms (Bobkova and Vorobyov, 2015; Grady et al., 2003)  
632 rather than reflecting healthy age-dependent changes.

633

634 It is noteworthy that a recent study in the McGill-R-Thy1-APP rat model of AD reported that  
635 neuroimaging biomarkers used in clinical AD research are valid in this transgenic model as well, even  
636 without clear neuronal loss or tauopathy (Leon et al., 2010; Parent et al., 2017). For example, they  
637 report early abnormal FC and cognitive deficits at 9-11 months of age prior to hypometabolism and  
638 A $\beta$  detected by PET imaging at 16-19 months of age. Additionally, progressive cognitive deficits as well  
639 as reduced hippocampal volume and CSF A $\beta_{1-42}$  were described (Parent et al., 2017). Together, these  
640 results seem to indicate that mainly the amyloid-driven synaptotoxic effects leads to a biomarker  
641 profile highly analogous of human AD. Nevertheless, although initial synaptic vulnerability to amyloid

642 toxicity might kick-start the disconnection cascade, the influence of consequent tauopathy cannot be  
643 ignored, especially when assessing potential therapeutic strategies. Therefore, the TgF344-AD rat  
644 model might be a better alternative to be used in future translational studies as this model also entails  
645 tauopathy as well as neuronal loss (Cohen et al., 2013). Discrepancies in results between the McGill-  
646 R-Thy1-APP and TgF344-AD rat could be explained by differences in experimental design, such as time  
647 points investigated but also use of anaesthesia. Whereas no early hyperconnectivity nor clear  
648 macroscopic volume loss was detected in the TgF344-AD rat model using the techniques described  
649 here, it is possible that these effects occurred outside the scope of this study, so future studies might  
650 examine the TgF344-AD rat model at both younger and older ages.

651

## 652 **CONCLUSION**

653 We have shown that striking FC dysfunction was the earliest detectable hallmark in the TgF344-AD rat  
654 model and that this preceded the presence of structural changes as assessed using the current  
655 methodology. Overall, the progressive aggravation of neuroimaging abnormalities, as well as the  
656 regions affected in the TgF344-AD rat model are in line with previous human AD research, which show  
657 pathological changes in posterior cingulate cortex, hippocampal areas and temporal lobes.  
658 Importantly, FC deficits were detected prior to significant amyloid plaque deposition, supporting the  
659 use of rsfMRI as an early non-invasive MRI marker reflecting underlying early-stage synaptic or  
660 neuronal dysfunction. The characterization of AD pathology in this rat model using highly translational  
661 MRI techniques highlights the potential of this model to be used in valuable future preclinical AD  
662 research.

663

## 664 **ACKNOWLEDGEMENTS**

665 This research was supported by the European Union's Seventh Framework Programme (FP7/2007-  
666 2013) under grant agreement number HEALTH-F2-2011-278850 (INMiND) and by the Fund for  
667 Scientific Research Flanders (FWO) (grant agreements G067515N and G057615N). The purchase of

668 the TgF344-AD rat was jointly supported by the European Union's Seventh Framework Programme  
669 (FP7/2007-2013) under grant agreement n° HEALTH-F2-2011-278850 (INMiND) and Alzheimer  
670 Research UK network funds. The Bruker Pharmascan 7T system (Bruker, Ettlingen, Germany) was  
671 funded through the Hercules Foundation Belgium (Grant Nr. AUHA/012) and in part by the Flemish  
672 Impulse funding for heavy scientific equipment (42/FA010100/123) granted to Prof. Dr. Annemie Van  
673 der Linden. The computational resources and services used in this work were provided by the HPC  
674 core facility CalcUA of the Universiteit Antwerpen, the VSC (Flemish Supercomputer Center), funded  
675 by the Hercules Foundation and the Flemish Government – department EWI. This research was further  
676 supported by the grants D-17/02/006-SUM and E-15/22/113-COS from the Paracelsus Medical  
677 University Research Fund PMU-FFF.

678

## 679 REFERENCES

- 680 Adamczak, J., et al., 2017. Neurogenesis upregulation on the healthy hemisphere after stroke  
681 enhances compensation for age-dependent decrease of basal neurogenesis. *Neurobiol Dis.*  
682 99, 47-57.
- 683 Arenaza-Urquijo, E. M., et al., 2013. Relationships between years of education and gray matter  
684 volume, metabolism and functional connectivity in healthy elders. *Neuroimage.* 83, 450-7.
- 685 Ashburner, J., Ridgway, G. R., 2012. Symmetric diffeomorphic modeling of longitudinal structural MRI.  
686 *Front Neurosci.* 6, 197.
- 687 Ashburner, J. R., G.R., Tensor-Based Morphometry. In: A. W. Toga, (Ed.), *Brain Mapping.* Academic  
688 Press, Waltham, 2015, pp. 383-394.
- 689 Badhwar, A., et al., 2017. Resting-state network dysfunction in Alzheimer's disease: A systematic  
690 review and meta-analysis. *Alzheimers Dement (Amst).* 8, 73-85.
- 691 Balachandar, R., et al., 2015. A study of structural and functional connectivity in early Alzheimer's  
692 disease using rest fMRI and diffusion tensor imaging. *Int J Geriatr Psychiatry.* 30, 497-504.
- 693 Barage, S. H., Sonawane, K. D., 2015. Amyloid cascade hypothesis: Pathogenesis and therapeutic  
694 strategies in Alzheimer's disease. *Neuropeptides.* 52, 1-18.
- 695 Bazzigaluppi, P., et al., 2017. Early-stage attenuation of phase-amplitude coupling in the hippocampus  
696 and medial prefrontal cortex in a transgenic rat model of Alzheimer's disease. *J Neurochem.*
- 697 Bobkova, N., Vorobyov, V., 2015. The brain compensatory mechanisms and Alzheimer's disease  
698 progression: a new protective strategy. *Neural Regen Res.* 10, 696-7.
- 699 Braak, H., Braak, E., 1991. Neuropathological stageing of Alzheimer-related changes. *Acta*  
700 *Neuropathol.* 82, 239-59.
- 701 Braak, H., Braak, E., 1995. Staging of Alzheimer's disease-related neurofibrillary changes. *Neurobiol*  
702 *Aging.* 16, 271-8; discussion 278-84.
- 703 Brun, A., Englund, E., 1986. A white matter disorder in dementia of the Alzheimer type: a  
704 pathoanatomical study. *Ann Neurol.* 19, 253-62.
- 705 Busche, M. A., et al., 2012. Critical role of soluble amyloid-beta for early hippocampal hyperactivity in  
706 a mouse model of Alzheimer's disease. *Proc Natl Acad Sci U S A.* 109, 8740-5.

707 Chase, A., 2014. Alzheimer disease: Altered functional connectivity in preclinical dementia. *Nat Rev*  
708 *Neurol.* 10, 609.

709 Cohen, R. M., et al., 2013. A transgenic Alzheimer rat with plaques, tau pathology, behavioral  
710 impairment, oligomeric abeta, and frank neuronal loss. *J Neurosci.* 33, 6245-56.

711 Daianu, M., et al., 2015. Multi-Shell Hybrid Diffusion Imaging (HYDI) at 7 Tesla in TgF344-AD Transgenic  
712 Alzheimer Rats. *PLoS One.* 10, e0145205.

713 Do Carmo, S., Cuello, A. C., 2013. Modeling Alzheimer's disease in transgenic rats. *Mol Neurodegener.*  
714 8, 37.

715 Dubois, B., et al., 2007. Research criteria for the diagnosis of Alzheimer's disease: revising the NINCDS-  
716 ADRDA criteria. *Lancet Neurol.* 6, 734-46.

717 Ewers, M., et al., 2011. Neuroimaging markers for the prediction and early diagnosis of Alzheimer's  
718 disease dementia. *Trends Neurosci.* 34, 430-42.

719 Gibbs, R. A., et al., 2004. Genome sequence of the Brown Norway rat yields insights into mammalian  
720 evolution. *Nature.* 428, 493-521.

721 Gold, B. T., et al., 2012. White matter integrity and vulnerability to Alzheimer's disease: preliminary  
722 findings and future directions. *Biochim Biophys Acta.* 1822, 416-22.

723 Gordon, J. A., 2011. Oscillations and hippocampal-prefrontal synchrony. *Curr Opin Neurobiol.* 21, 486-  
724 91.

725 Grady, C. L., et al., 2003. Evidence from functional neuroimaging of a compensatory prefrontal  
726 network in Alzheimer's disease. *J Neurosci.* 23, 986-93.

727 Grandjean, J., et al., 2014a. Optimization of anesthesia protocol for resting-state fMRI in mice based  
728 on differential effects of anesthetics on functional connectivity patterns. *Neuroimage.* 102 Pt  
729 2, 838-47.

730 Grandjean, J., et al., 2014b. Early alterations in functional connectivity and white matter structure in  
731 a transgenic mouse model of cerebral amyloidosis. *J Neurosci.* 34, 13780-9.

732 Hamaide, J., et al., 2017. Exploring sex differences in the adult zebra finch brain: In vivo diffusion tensor  
733 imaging and ex vivo super-resolution track density imaging. *Neuroimage.* 146, 789-803.

734 Hardy, J. A., Higgins, G. A., 1992. Alzheimer's disease: the amyloid cascade hypothesis. *Science.* 256,  
735 184-5.

736 Hoozemans, J. J., et al., 2006. Neuroinflammation and regeneration in the early stages of Alzheimer's  
737 disease pathology. *Int J Dev Neurosci.* 24, 157-65.

738 Jacob, H. J., Kwitek, A. E., 2002. Rat genetics: attaching physiology and pharmacology to the genome.  
739 *Nat Rev Genet.* 3, 33-42.

740 Johnson, K. A., et al., 2012. Brain imaging in Alzheimer disease. *Cold Spring Harb Perspect Med.* 2,  
741 a006213.

742 Jonckers, E., et al., 2011. Functional connectivity fMRI of the rodent brain: comparison of functional  
743 connectivity networks in rat and mouse. *PLoS One.* 6, e18876.

744 Joo, I. L., et al., 2017. Early neurovascular dysfunction in a transgenic rat model of Alzheimer's disease.  
745 *Sci Rep.* 7, 46427.

746 Leech, R., Sharp, D. J., 2014. The role of the posterior cingulate cortex in cognition and disease. *Brain.*  
747 137, 12-32.

748 Leon, W. C., et al., 2010. A novel transgenic rat model with a full Alzheimer's-like amyloid pathology  
749 displays pre-plaque intracellular amyloid-beta-associated cognitive impairment. *J Alzheimers*  
750 *Dis.* 20, 113-26.

751 Mucke, L., Selkoe, D. J., 2012. Neurotoxicity of amyloid beta-protein: synaptic and network  
752 dysfunction. *Cold Spring Harb Perspect Med.* 2, a006338.

753 Munoz-Moreno, E., et al., 2018. Early brain connectivity alterations and cognitive impairment in a rat  
754 model of Alzheimer's disease. *Alzheimers Res Ther.* 10, 16.

755 Nasrallah, F. A., et al., 2016. Functional connectivity MRI tracks memory networks after maze learning  
756 in rodents. *Neuroimage.* 127, 196-202.

757 Nir, T. M., et al., 2013. Effectiveness of regional DTI measures in distinguishing Alzheimer's disease,  
758 MCI, and normal aging. *Neuroimage Clin.* 3, 180-95.

759 Paasonen, J., et al., 2018. Functional connectivity under six anesthesia protocols and the awake  
760 condition in rat brain. *Neuroimage.* 172, 9-20.

761 Parent, M. J., et al., 2017. Multimodal Imaging in Rat Model Recapitulates Alzheimer's Disease  
762 Biomarkers Abnormalities. *J Neurosci.* 37, 12263-12271.

763 Paxinos, G., Watson, C., *The Rat Brain in Stereotaxic Coordinates.* 123Library. Academic Press, 2007.

764 Peca, S., et al., 2013. Neurovascular decoupling is associated with severity of cerebral amyloid  
765 angiopathy. *Neurology.* 81, 1659-65.

766 Pentkowski, N. S., et al., 2018. Anxiety-like behavior as an early endophenotype in the TgF344-AD rat  
767 model of Alzheimer's disease. *Neurobiol Aging.* 61, 169-176.

768 Princz-Kranz, F. L., et al., 2010. Vascular response to acetazolamide decreases as a function of age in  
769 the arcA beta mouse model of cerebral amyloidosis. *Neurobiol Dis.* 40, 284-92.

770 Quiroz, Y. T., et al., 2015. Brain Imaging and Blood Biomarker Abnormalities in Children With  
771 Autosomal Dominant Alzheimer Disease: A Cross-Sectional Study. *JAMA Neurol.* 72, 912-9.

772 Rao, J. S., et al., 2012. Neuroinflammation and synaptic loss. *Neurochem Res.* 37, 903-10.

773 Rorabaugh, J. M., et al., 2017. Chemogenetic locus coeruleus activation restores reversal learning in a  
774 rat model of Alzheimer's disease. *Brain.* 140, 3023-3038.

775 Sampath, D., et al., 2017. Cognitive dysfunction in major depression and Alzheimer's disease is  
776 associated with hippocampal-prefrontal cortex dysconnectivity. *Neuropsychiatr Dis Treat.* 13,  
777 1509-1519.

778 Schindelin, J., et al., 2012. Fiji: an open-source platform for biological-image analysis. *Nat Methods.* 9,  
779 676-82.

780 Scholvinck, M. L., et al., 2010. Neural basis of global resting-state fMRI activity. *Proc Natl Acad Sci U S*  
781 *A.* 107, 10238-43.

782 Selkoe, D. J., 2001. Alzheimer's disease: genes, proteins, and therapy. *Physiol Rev.* 81, 741-66.

783 Selkoe, D. J., 2002. Alzheimer's disease is a synaptic failure. *Science.* 298, 789-91.

784 Shah, D., et al., 2016a. Cholinergic and serotonergic modulations differentially affect large-scale  
785 functional networks in the mouse brain. *Brain Struct Funct.* 221, 3067-79.

786 Shah, D., et al., 2016b. Early pathologic amyloid induces hypersynchrony of BOLD resting-state  
787 networks in transgenic mice and provides an early therapeutic window before amyloid plaque  
788 deposition. *Alzheimers Dement.* 12, 964-976.

789 Shankar, G. M., et al., 2007. Natural oligomers of the Alzheimer amyloid-beta protein induce reversible  
790 synapse loss by modulating an NMDA-type glutamate receptor-dependent signaling pathway.  
791 *J Neurosci.* 27, 2866-75.

792 Sheline, Y. I., Raichle, M. E., 2013. Resting state functional connectivity in preclinical Alzheimer's  
793 disease. *Biol Psychiatry.* 74, 340-7.

794 Sigurdsson, T., Duvarci, S., 2015. Hippocampal-Prefrontal Interactions in Cognition, Behavior and  
795 Psychiatric Disease. *Front Syst Neurosci.* 9, 190.

796 Smith, L. A., McMahon, L. L., 2018. Deficits in synaptic function occur at medial perforant path-dentate  
797 granule cell synapses prior to Schaffer collateral-CA1 pyramidal cell synapses in the novel  
798 TgF344-Alzheimer's Disease Rat Model. *Neurobiol Dis.* 110, 166-179.

799 Stebbins, G. T., Murphy, C. M., 2009. Diffusion tensor imaging in Alzheimer's disease and mild cognitive  
800 impairment. *Behav Neurol.* 21, 39-49.

801 Thal, D. R., et al., 2002. Phases of A beta-deposition in the human brain and its relevance for the  
802 development of AD. *Neurology.* 58, 1791-800.

803 van den Heuvel, M. P., Hulshoff Pol, H. E., 2010. Exploring the brain network: a review on resting-state  
804 fMRI functional connectivity. *Eur Neuropsychopharmacol.* 20, 519-34.

805 Voorhees, J. R., et al., 2017. (-)-P7C3-S243 Protects a Rat Model of Alzheimer's Disease From  
806 Neuropsychiatric Deficits and Neurodegeneration Without Altering Amyloid Deposition or  
807 Reactive Glia. *Biol Psychiatry.*

808 Weaver, K. E., et al., 2016. Directional patterns of cross frequency phase and amplitude coupling  
809 within the resting state mimic patterns of fMRI functional connectivity. *Neuroimage*. 128, 238-  
810 251.

811 Weston, P. S., et al., 2015. Diffusion imaging changes in grey matter in Alzheimer's disease: a potential  
812 marker of early neurodegeneration. *Alzheimers Res Ther*. 7, 47.

813 Zhang, Y., et al., 2001. Segmentation of brain MR images through a hidden Markov random field model  
814 and the expectation-maximization algorithm. *IEEE Transactions on Medical Imaging*. 20, 45-  
815 57.

816

817

818



819 **TABLES AND FIGURES**

820 **TABLE 1**

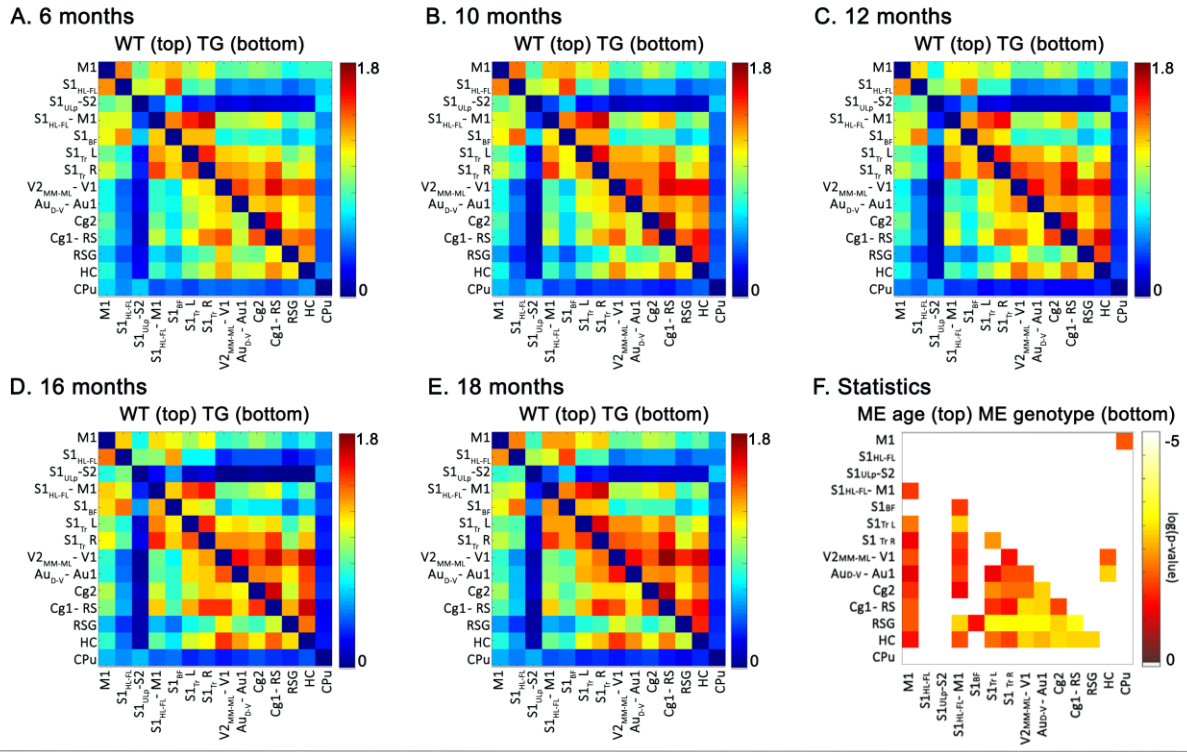
821

| <b>Abbreviation</b>   | <b>Region</b>   | <b>Abbreviation</b>     | <b>Region</b>  |
|-----------------------|---|-------------------------|--|
| M1                    | Primary motor cortex  | V2 <sub>MM-ML</sub> /V1 | Secondary visual cortex, mediomedial and mediolateral area / Primary visual cortex |
| S1 <sub>HFL</sub>     | Primary somatosensory cortex, forelimb and hindlimb region                        | Aud-v/Au1               | Secondary auditory cortex, dorsal and ventral area / Primary auditory cortex       |
| S1 <sub>ULp</sub> /S2 | Primary somatosensory cortex, upper lip region / Secondary somatosensory cortex   | Cg2                     | Cingulate cortex, area 2   |
| S1 <sub>HFL</sub> /M1 | Primary somatosensory cortex, forelimb and hindlimb region / Primary motor cortex | Cg1/RS                  | Cingulate cortex, area 1 / Retrosplenial cortex                                    |
| S1 <sub>BF</sub>      | Primary somatosensory region, barrel field  | RSG                     | Retrosplenial granular cortex  |
| S1 <sub>Tr</sub> L    | Primary somatosensory cortex, trunk region, left                                  | HC                      | Hippocampus  |
| S1 <sub>Tr</sub> R    | Primary somatosensory cortex, trunk region, right                                 | CPu                     | Caudate putamen  |

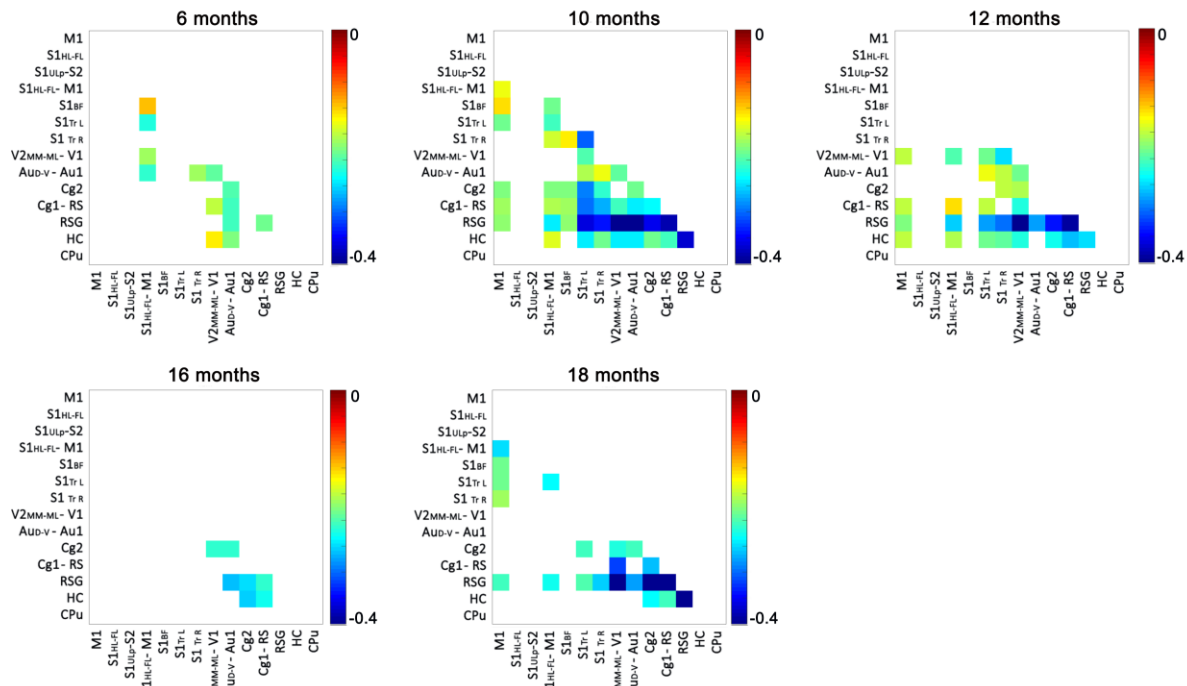
822 **Table 1. Overview of the main regions obtained from the anatomically relevant ICA components.**

823

824



**G. Post hoc statistics:  $\Delta$ FC (TG < WT)**



825

826

**Figure 1. Inter-regional FC analysis. A-E.** Every matrix shows the average z-transformed functional

827

connectivity (zFC) for both WT (top half) and TG (bottom half) animals. Each square indicates the zFC

828

between a pair of ROIs. The colour scale represents the strength of the connectivity with green/blue

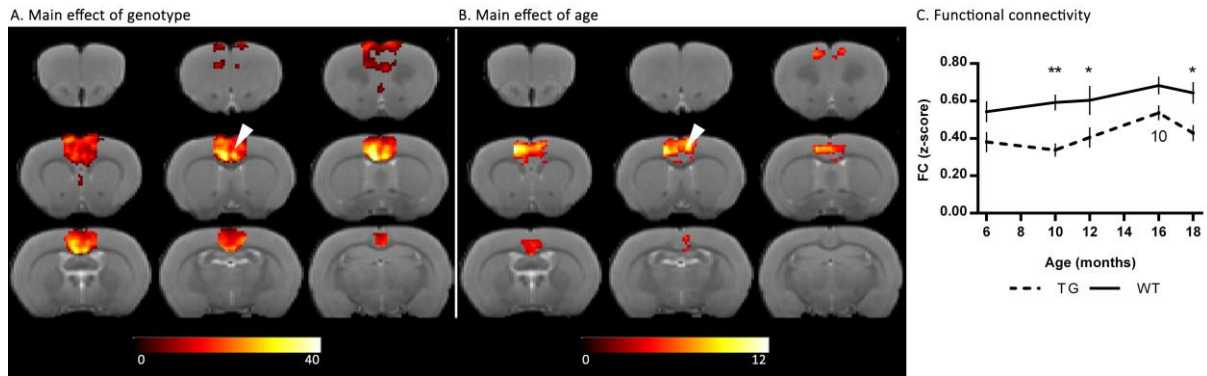
829

indicating a low zFC and yellow/red indicating higher zFC values. Abbreviations of regions: see Table

830 1. **F.** Main outcome of the statistical analysis. No significant [age x genotype] interaction was found  
831 below the FDR correction of  $p < 0.05$ , so only significant main effects are reported. The bottom half of  
832 the matrix shows the main effect of genotype (TG < WT), whereas the main effect of age is shown in  
833 the top half of the matrix. The colour scale represents the  $\log(p\text{-value})$ , with yellow indicating a lower  
834 p-value. **G.** Results of the *post hoc* tests showing significantly reduced FC in TG animals. The colour  
835 scale indicates the difference ( $\Delta FC$ ) between WT and TG (corresponding to significant p-values,  
836  $p < 0.05$ ) with blue indicating a stronger decrease in TG animals compared to WT.

837

838



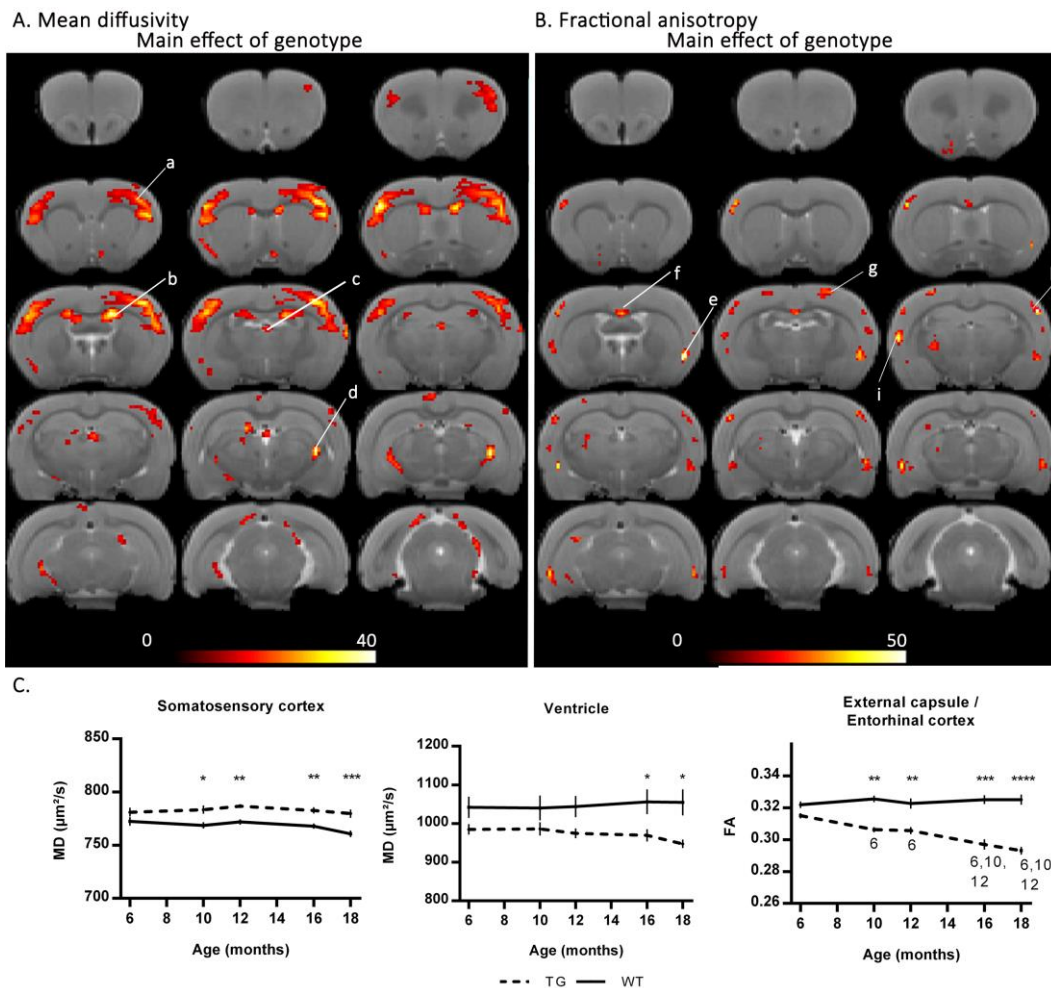
839

840 **Figure 2. Intra-regional FC analysis for the frontal cingulate cortex by means of a seed based analysis.**

841 **A-B.** Outcome of a voxel-based analysis of the Cg2 FC maps, with arrowheads indicating the location  
 842 of the seed (four voxels). A main effect of genotype (A, TG<WT) is present throughout the region,  
 843 whereas only a small cluster shows an age-dependent alteration (B). Note that this age-dependent  
 844 change was mainly driven by an increase of FC between 10 and 16 months in TG animals (C). The  
 845 colour scale represents f-values with yellow indicating a larger difference between the conditions  
 846 investigated. All results are shown on an anatomical 3D-template, FDR-corrected  $p < 0.05$  and a  
 847 minimum cluster size of 10 voxels. **C.** Evolution of FC within the restrictions of the cluster showing a  
 848 main effect of genotype (A). Stars indicate significant differences between TG and WT, with  $*p < 0.05$ ;  
 849  $** p < 0.01$ . Age-dependent alterations are indicated with numbers representing significant differences  
 850 compared to the indicated time point (e.g. '6' indicates a significant difference between that  
 851 respective time point and the 6 month time point of the same group).

852

853



854

855 **Figure 3. Voxel-based statistical analysis of DTI parameters, MD and FA.** Significant main effects of

856 genotype are shown for both MD (A) and FA (B). Results are displayed on an anatomical template,

857 with a visualization threshold of FDR  $p < 0.05$  and a minimum cluster size of 10 voxels. The colour scale

858 indicates f-values with yellow indicating a larger difference between the conditions investigated. a.

859 Primary motor and somatosensory cortex (M1, M2, S1<sub>HL-FL</sub>; S1<sub>ULp</sub>); b. Lateral ventricle; c. Third

860 ventricle; d. Subgeniculate nucleus; e. External capsule/entorhinal cortex; f. corpus callosum; g.

861 Sensorimotor cortex (M1, S1<sub>HL-FL</sub>); h. Somatosensory cortex (S1<sub>BF</sub>, S1<sub>HL-FL</sub>); i. Lateral somatosensory

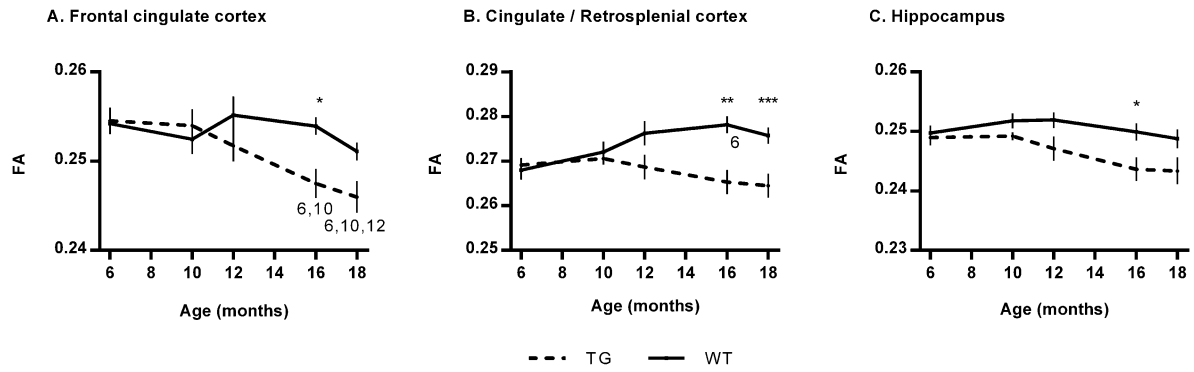
862 cortex (S2, S1<sub>ULp</sub>). C. The strongest effects according to the VBA are plotted in graphs. Stars indicate

863 significant differences between TG and WT, with \* $p < 0.05$ ; \*\* $p < 0.01$ ; \*\*\* $p < 0.001$ ; \*\*\*\* $p < 0.0001$ . Age-

864 dependent alterations are indicated with numbers representing significant differences compared to

865 the indicated time point (e.g. '6' indicates a significant difference between that respective time point

866 and the 6 month time point of the same group).



867

868 **Figure 4. ROI-based analysis of FA in regions characteristically involved in AD.** Stars indicate

869 significant differences between TG and WT, with \* $p < 0.05$ ; \*\* $p < 0.01$ ; \*\*\* $p < 0.001$ . Age-dependent

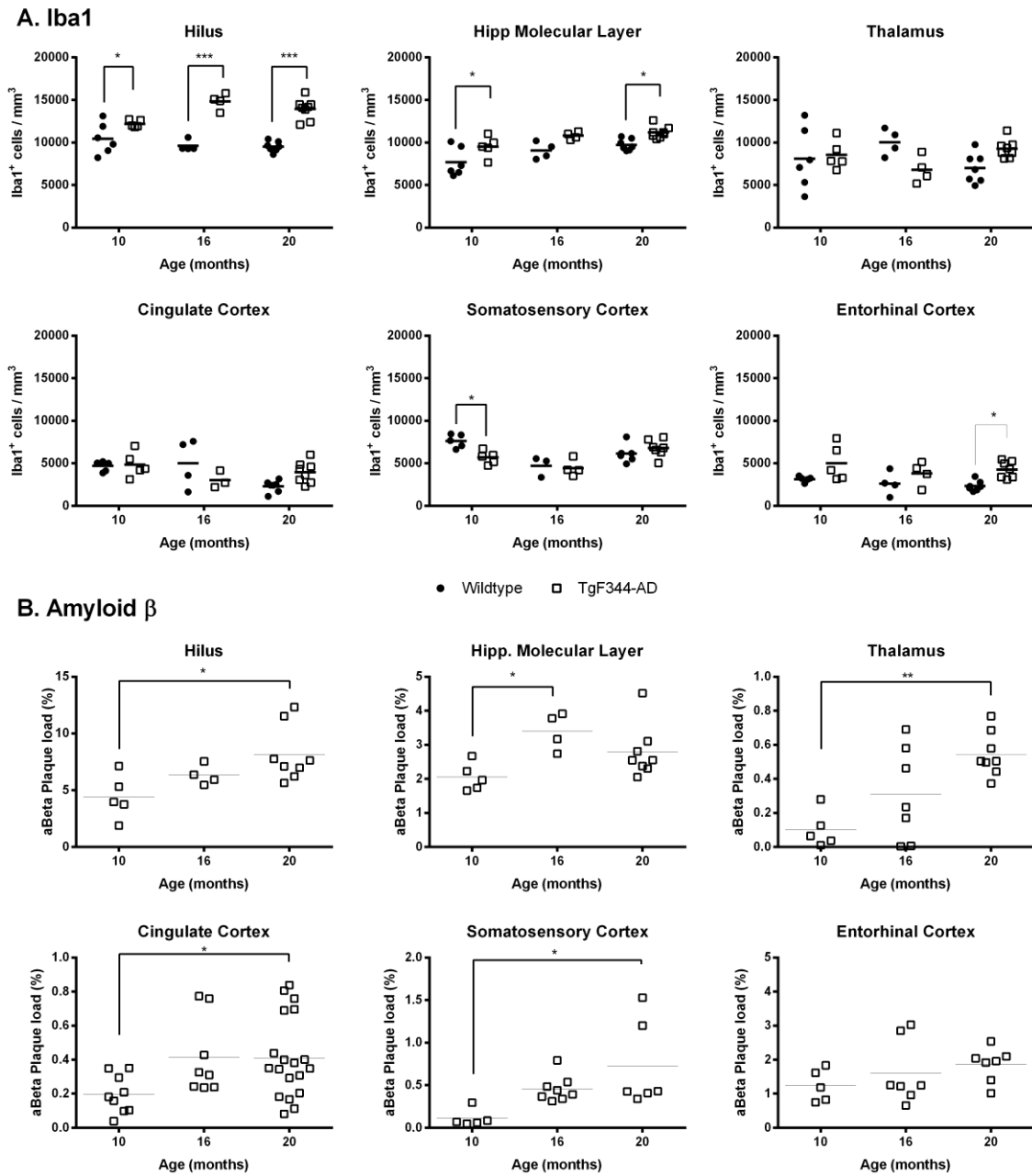
870 alterations are indicated with numbers representing significant differences compared to the indicated

871 time point (e.g. '6' indicates a significant difference between that respective time point and the 6

872 month time point of the same group).

873

874



875

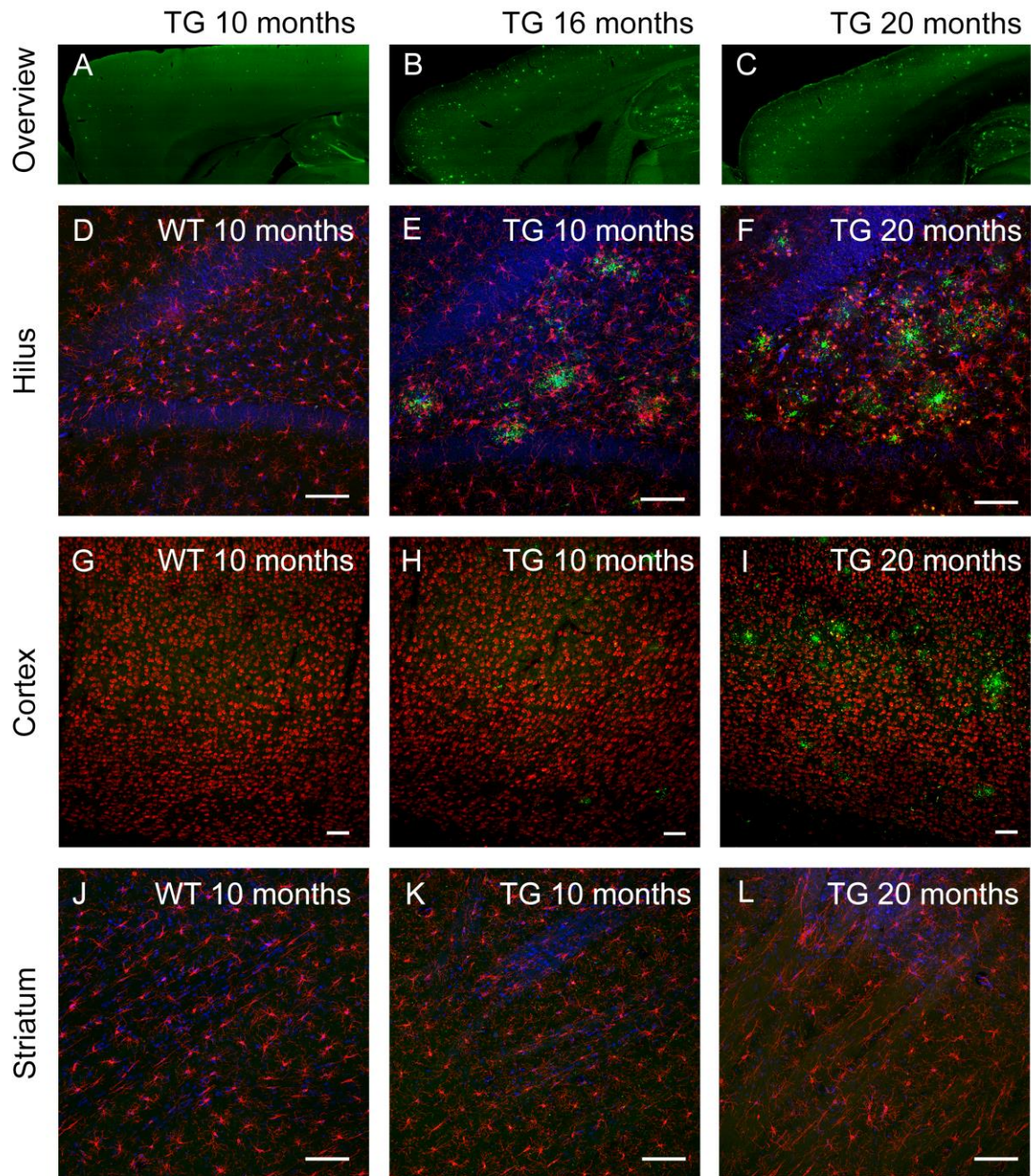
876 **Figure 5. Quantification of Iba1-expressing microglia (A) and amyloid  $\beta$  load (B) in various regions. \***

877  $p < 0.05$ ; \*\*  $p < 0.01$ .

878

879

880



881

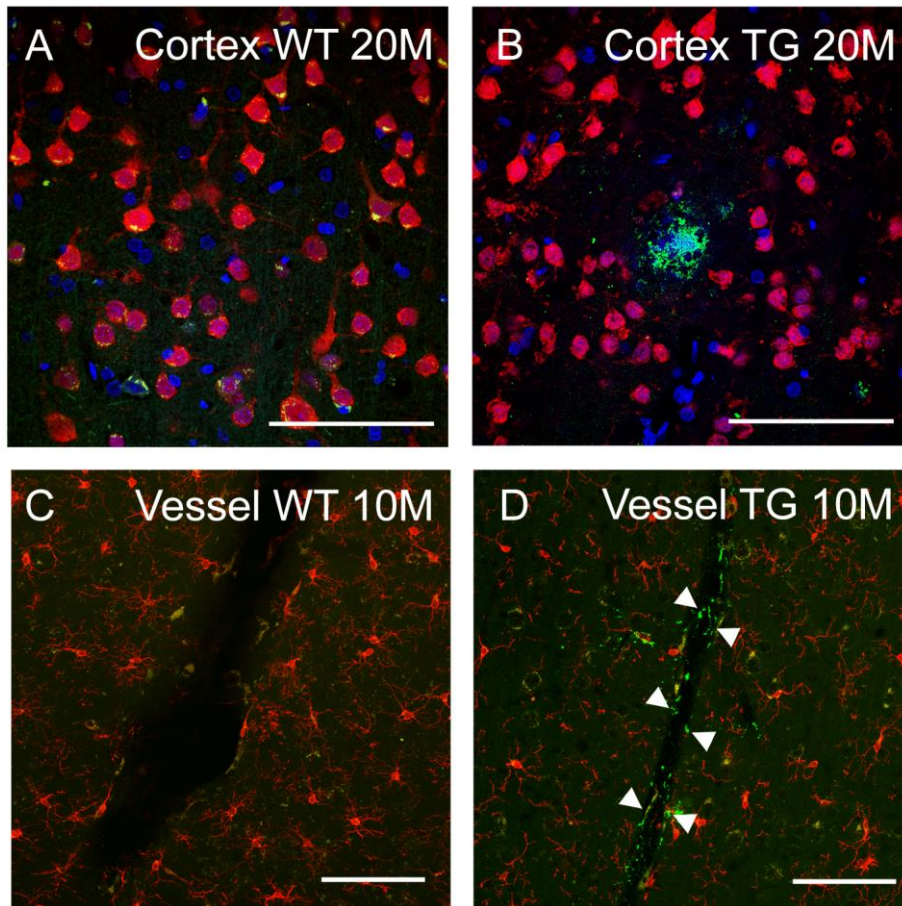
882 **Figure 6. Illustrative images of *ex vivo* AD pathology.** A-C. Overview showing the increase in amyloid  
 883  $\beta$  plaque load in the cortical regions of a 10 month, 16 month and 20 month old TG rat. D-F. Age-  
 884 dependent increase in microglia (Iba1, red) and amyloid  $\beta$  (green) in 10 month and 20 month old TG  
 885 rats, as compared to a 10 month old WT rat (nuclear counterstain DAPI in blue). G-I. Age-dependent  
 886 increase of plaque load (amyloid  $\beta$ , green) in the cingulate cortex, without clear evidence of neuronal  
 887 loss (NeuN, red) in 10 month and 20 month old TG rats, as compared to a 10 month old WT rat. J-L.



888 The striatum did not present significant increase in microglia (Iba1, red) and amyloid  $\beta$  (green) in 10  
889 month and 20 month old TG rats, as compared to a 10 month old WT rat (nuclear counterstain DAPI  
890 in blue).

891

892



893

894 **Figure 7. Illustrative images of neuronal density and cerebral amyloid angiopathy. A-B.** Decrease in  
 895 the neuronal density (NeuN, red) around an amyloid  $\beta$  plaque (green) localized in the somatosensory  
 896 cortex in 20 month old TG rats as compared to a 20 month old WT rat. **N-O.** Already at 10 months, the  
 897 walls of blood vessels in the TG rats, but not WT, showed evidence for cerebral amyloid angiopathy  
 898 (amyloid  $\beta$ , green). Surrounding microglia are detected with Iba1 (red). Arrowheads indicate the  
 899 showing amyloid  $\beta$  positive staining on blood vessel walls. Scale bars: 100  $\mu$ m.